

DRUG TOXICITY

Multiscale profiling of tyrosine kinase inhibitor cardiotoxicity reveals mechanosensitive ion channel PIEZO1 as cardioprotective

Amit Manhas^{1,2†}, Yu Liu^{1,2†}, Chikage Noishiki^{1,3}, David Wu^{1,3}, Dipti Tripathi^{1,3,4}, Sarah Mirza^{1,3}, Dilip Thomas^{1,2}, Lu Liu^{1,3}, Avirup Guha⁵, Patricia K. Nguyen^{1,2}, Ian Y. Chen^{1,2}, Vipul Chitalia⁶, Paul Cheng^{1,2}, Danish Sayed⁷, Melinda L. Telli⁸, Karim Sallam^{1,2}, Joseph C. Wu^{1,2,9}, Nazish Sayed^{1,2,3,4*}

Copyright © 2025 The Authors, some rights reserved; exclusive licensee American Association for the Advancement of Science. No claim to original U.S. Government Works

Tyrosine kinase inhibitors (TKIs) have improved cancer outcomes but are limited by cardiovascular toxicity, most notably hypertension and heart failure. The underlying mechanisms remain poorly understood, hindering the development of protective strategies. Here, we investigated the role of endothelial mechanotransduction in mediating vascular and cardiac injury caused by the vascular endothelial growth factor receptor–targeting TKI sunitinib. Using patient-specific induced pluripotent stem cell–derived endothelial cells (iPSC-ECs) and a mouse model of TKI-induced hypertension, we identified down-regulation of piezo-type mechanosensitive ion channel component 1 (*PIEZO1*), a mechanically activated ion channel, as a driver of endothelial dysfunction. Restoring *PIEZO1* expression, either pharmacologically with Yoda1, a selective agonist, or through inducible overexpression in iPSC-ECs, reversed sunitinib-induced endothelial dysfunction and mitigated its hypertensive effects, providing both mechanistic and genetic validation of *PIEZO1*'s protective role against vascular toxicity. In mice, cotreatment with sunitinib and Yoda1 prevented the long-term cardiac dysfunction observed after sunitinib exposure and normalized elevations in circulating cardiac stress biomarkers. Single-nucleus multiomic profiling of mouse hearts revealed that sunitinib exposure activated chromatin remodeling and fibrogenic programs, which were reversed with *PIEZO1* activation. Human engineered cardiac organoids further demonstrated that sunitinib impaired cardiomyocyte function only in the presence of endothelial cells, confirming a role for disrupted endothelial–cardiomyocyte cross-talk in TKI cardiotoxicity. Together, these findings identify endothelial *PIEZO1* as a mediator of TKI-induced hypertension and cardiac dysfunction and highlight *PIEZO1* activation as a potential therapeutic strategy for protecting cardiovascular health during cancer therapy.

INTRODUCTION

Advances in cancer therapies have markedly improved survival, with an estimated 50 million cancer survivors worldwide (1). Among these, tyrosine kinase inhibitors (TKIs) have contributed substantially, helping drive 5-year cancer survival rates to more than 68% (2). Although generally associated with fewer side effects than traditional chemotherapy, TKIs are increasingly recognized for their vasculotoxicity (3), which can cause lasting cardiovascular damage (4). TKIs function by inhibiting overactive tyrosine kinase pathways in cancer cells (5), yet nearly all of the 50 TKIs in clinical use have been linked to cardiovascular events (6). For example, nilotinib, vandetanib, and pazopanib have been associated with vascular toxicity, including arterial thrombosis and hypertension (7). Similarly, vascular endothelial

growth factor receptor (VEGFR)-targeting TKIs such as sunitinib, sorafenib, and ponatinib are strongly associated with hypertension and heart failure (8). Despite their efficacy in controlling tumor progression, VEGFR-TKIs can precipitate severe cardiovascular events including left ventricular dysfunction, arrhythmias, stroke, and sudden cardiac death (9). Understanding the impact of these therapies on cardiovascular health is essential for developing strategies to mitigate their long-term complications.

Endothelial cells (ECs), which line blood vessels and regulate vascular tone through paracrine signaling, are particularly susceptible to cancer therapy–induced injury (10, 11). Under physiological conditions, ECs maintain a balance between vasodilation and vasoconstriction. VEGFR-TKIs disrupt this balance, promoting vascular remodeling, arterial stiffness, and impaired nitric oxide (NO) synthesis (12). Sunitinib, for example, has been shown to down-regulate the nitric oxide synthase 3 (NOS3)–NO pathway and increase oxidative stress and production of vasoconstrictors, such as endothelin-1 (13). Hypertension after sunitinib treatment has been observed in both patients and animal models (14, 15), supporting a mechanistic link between TKI-induced EC dysfunction and hypertension. Despite these insights, the molecular basis of VEGFR-TKI–mediated EC injury remains poorly defined. ECs have a highly specialized mechanotransduction system that senses hemodynamic forces such as shear stress (16). This sensing is mediated by specialized mechanosensors, including ion channels, receptors, adhesion molecules, and glycoproteins, which regulate downstream signaling, gene

¹Stanford Cardiovascular Institute, Stanford University School of Medicine, Stanford, CA 94305, USA. ²Division of Cardiology, Department of Medicine, Stanford University School of Medicine, Stanford, CA 94305, USA. ³Division of Vascular Surgery, Department of Surgery, Stanford University School of Medicine, Stanford, CA 94305, USA. ⁴Baszucki Family Vascular Surgery Biobank, Stanford University School of Medicine, Stanford, CA 94305, USA. ⁵Department of Medicine, Division of Cardiology, and Vascular Biology Center, Medical College of Georgia at Augusta University, Augusta, GA 30912, USA. ⁶Renal Section, Department of Medicine, Boston University School of Medicine, Boston, MA 02118, USA. ⁷Department of Cell Biology and Molecular Medicine, Rutgers New Jersey Medical School, Newark, NJ 07103, USA. ⁸Division of Oncology, Department of Medicine, Stanford University School of Medicine, Stanford, CA 94305, USA. ⁹Greenstone Biosciences, Palo Alto, CA 94304, USA.

†These authors contributed equally to this work.

*Corresponding author. Email: sayedns@stanford.edu

expression, and vascular responses (17). VEGFR-TKIs may impair this system, resulting in endothelial dysfunction and hypertension.

Chronic hypertension, in turn, can progress to hypertensive heart disease, characterized by myocardial stiffness, cardiomyocyte (CM) hypertrophy, and myocardial fibrosis (18, 19). Long-term VEGFR-TKI therapy has been associated with adverse outcomes, including heart failure, myocardial infarction, and arrhythmias (3, 20), and studies further implicate VEGFR-TKIs in CM apoptosis and impaired contractility (21–25). Given the strong interplay among EC dysfunction, hypertension, and heart failure, unraveling their mechanistic connections is crucial. In this study, we used patient-specific induced pluripotent stem cell (iPSC)-derived ECs and a mouse model of TKI-induced cardiotoxicity to show that impaired mechanotransduction, driven by down-regulation of the mechanically activated ion channel PIEZO1, mediates EC dysfunction and TKI-induced hypertension.

RESULTS

Patients treated with VEGFR-TKIs exhibit hypertension and endothelial dysfunction

VEGFR-targeting TKIs are associated with hypertension, likely because of effects on vascular regression and enhanced vasoconstrictor signaling, with incidence rates reported as high as 40% in first-time users (26–30). Hypertension may arise from both on-target and off-target effects of TKIs on the endothelium (13). To investigate the mechanistic link between TKI-induced hypertension and EC dysfunction, we recruited a cohort of patients with cancer ($n = 28$) who developed hypertension after TKI therapy, along with healthy controls (HCs; $n = 5$) who had not received TKIs (tables S1 and S2 and Fig. 1A). Serial blood pressure measurements revealed a significant rise in systolic blood pressure during TKI treatment compared with baseline values (Fig. 1B and fig. S1, A and B; $P < 0.0001$). To assess clinical endothelial function, we measured reactive hyperemia using EndoPAT digital plethysmography (31, 32). The reactive hyperemia index (RHI), where values >1.67 denote normal endothelial function, was significantly reduced in TKI-treated patients compared with HCs (Fig. 1, C and D, and fig. S1C; $P = 0.0348$). Endothelial dysfunction was observed even in the absence of other vascular comorbidities such as atherosclerosis, suggesting a direct and independent effect of VEGFR-TKIs on endothelial physiology (tables S1 and S2).

Patient-specific iPSC-ECs exposed to VEGFR-TKIs exhibit dysfunction

Given the limited availability of patient vascular tissues, we established an iPSC-based platform to model TKI-associated endothelial toxicity in a patient-specific manner (33, 34). iPSC clones were generated from all 28 TKI-treated patients and 5 HCs and differentiated into ECs using a chemically defined protocol (fig. S1, D and E) (35). These iPSC-ECs displayed the typical “cobblestone” morphology of EC monolayers. To assess vasculotoxicity across VEGFR-TKIs, we conducted a high-throughput viability screen using PrestoBlue to identify agents with the strongest cytotoxic effects and to establish an optimal dosing strategy that allowed modeling of drug effects on iPSC-ECs without inducing cell death. Of the 10 VEGFR-TKIs tested, ponatinib, sorafenib, and sunitinib induced the strongest cytotoxic effects compared with vehicle controls (fig. S1F). Dose-response studies revealed that sunitinib produced the most pronounced down-regulation of endothelial markers, including *PECAM1*, *CDH5*, and

NOS3, even at 0.1 μ M (fig. S2A). A time-course study demonstrated that maximal suppression of endothelial markers occurred at day 7 of treatment (fig. S2B). Next, we characterized iPSC-ECs derived from all 28 TKI-treated patients and HCs after sunitinib exposure (Fig. 1E). Compared with vehicle-treated controls, sunitinib-treated iPSC-ECs exhibited impaired endothelial function, including defective tube formation (Fig. 1F and fig. S2C), reduced NO production in response to acetylcholine (Fig. 1G and fig. S2D), and diminished uptake of acetylated low-density lipoprotein (LDL) (fig. S2, E and F). These findings indicated that sunitinib directly impairs key endothelial signaling pathways.

To elucidate molecular mechanisms, we performed bulk RNA sequencing (RNA-seq) on iPSC-ECs from 12 TKI-treated patients after exposure to sunitinib or vehicle. Principal components analysis showed strong clustering by the treatment group (fig. S3A) but exhibited differentially expressed genes (DEGs) between the vehicle- and sunitinib-treated groups (Fig. 1H). Enrichment analysis indicated up-regulation of cell death and collagen formation pathways (fig. S2E) and down-regulation of pathways linked to endothelial mechanotransduction, including responses to fluid shear stress and mechanical stimuli, focal adhesion signaling, and vascular smooth muscle cell (SMC) contraction (Fig. 1I). Consistently, sunitinib-treated iPSC-ECs showed reduced expression of key endothelial markers, including *VEGFR2/3*, *PECAM1*, and *CDH5* (Fig. 1J), which are critical for maintaining endothelial integrity and mechanotransduction capacity (36, 37). Deeper analysis revealed suppression of multiple mechanotransduction-associated genes, including glycocalyx-related (*HAS2* and *CSPG4*) and mechanosensitive ion channels (*TRPV4*, *PIEZO1*, and *PIEZO2*), heterotrimeric guanine nucleotide-binding protein-coupled receptors (*GPR68* and *BDKRB2*), and receptor tyrosine kinases (*TIE1*) (Fig. 1K and fig. S3C). Together, these findings suggested that VEGFR-TKIs disrupt endothelial mechanotransduction, rendering ECs unable to sense and adapt to hemodynamic forces and thereby predisposing to vascular dysfunction and remodeling.

Sunitinib disrupts EC function and mechanotransduction pathways in primary ECs

To determine whether the endothelial dysfunction observed in iPSC-ECs was consistent across primary EC subtypes, we exposed human aortic ECs and human cardiac microvascular ECs to sunitinib (fig. S4A). Consistent with our iPSC-EC findings, both human aortic ECs and human cardiac microvascular ECs displayed impaired function, including reduced tube formation and NO production (fig. S4, B and C). Bulk RNA-seq revealed distinct transcriptional signatures within each treatment group (fig. S4D). Gene Ontology (GO) analysis highlighted down-regulation of pathways central to endothelial mechanotransduction, such as cellular responses to shear stress, focal adhesion signaling, and regulation of vascular tone (fig. S4E). Classical endothelial markers, including *PECAM1*, *CDH5*, and *NOS3*, were reduced in sunitinib-treated cells relative to controls (fig. S4F), and core mechanotransduction genes, including *PIEZO1*, *TRPV4*, *TIE1*, and *GPR68*, were down-regulated (fig. S4G). These results demonstrated that sunitinib induces a consistent, subtype-independent disruption of endothelial function and mechanosensing pathways.

To test whether these *in vitro* phenotypes reflected the *in vivo* endothelial status of patients, we isolated blood endothelial progenitor cells (BECs) from three patients with cancer receiving sunitinib therapy (Pt. 1, Pt. 2, and Pt. 3) and from one HC (fig. S5A). BECs from sunitinib-treated patients exhibited down-regulation of *PECAM1*

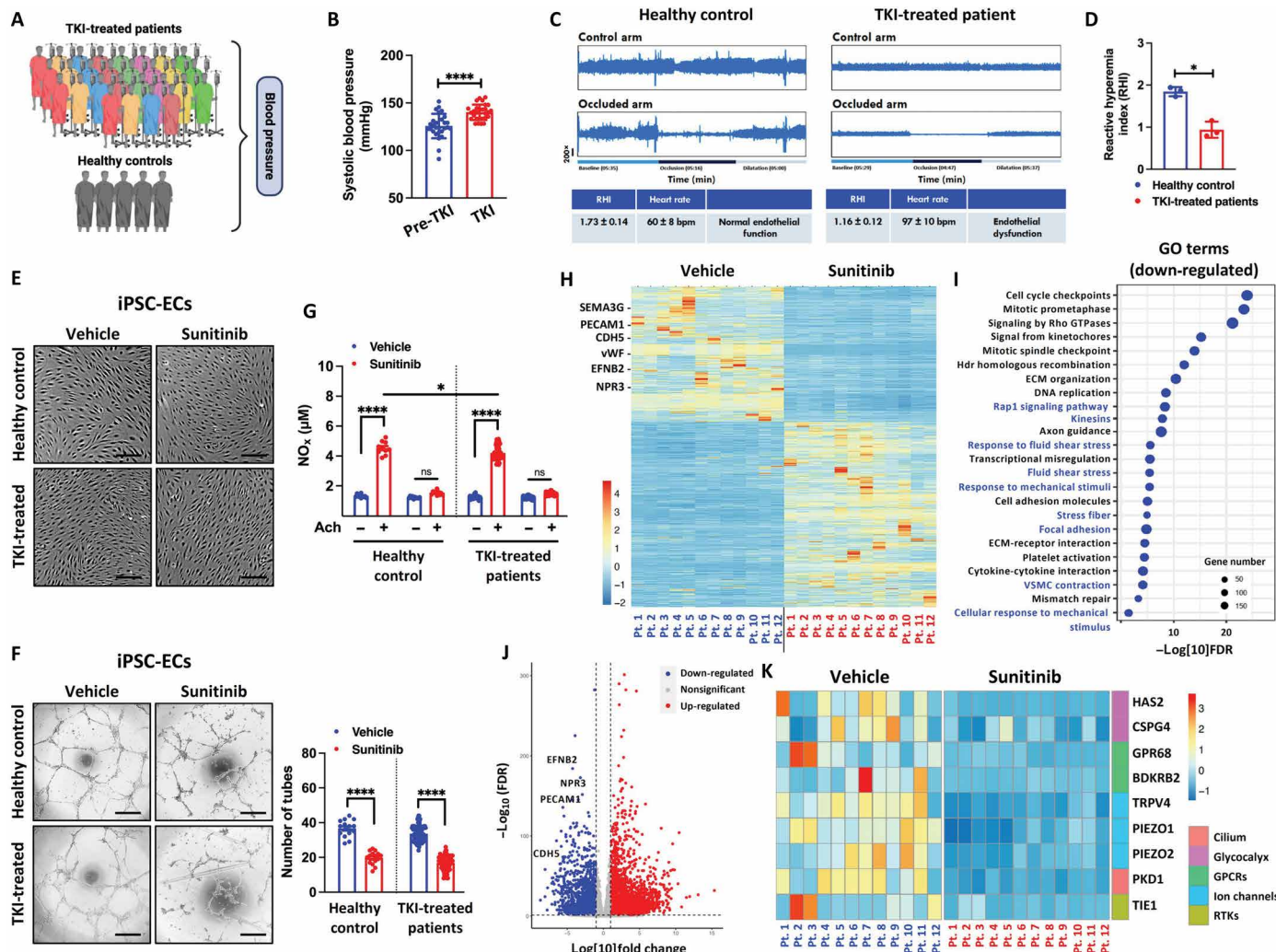


Fig. 1. Patients treated with TKIs exhibit hypertension and impaired endothelial function. (A) Schematic of patient recruitment workflow for TKI-treated patients and HCs. Schematic created using BioRender. (B) Systolic blood pressure in patients before and during TKI treatment ($n = 28$ patients). (C) Representative EndoPAT traces showing RHI in HCs (left) and TKI-treated patients (right). (D) Quantification of RHI in HCs and TKI-treated patients ($n = 3$ patients per group). (E) Bright-field images of iPSC-ECs from HCs and TKI-treated patients after exposure to vehicle or sunitinib, showing “cobblestone” morphology. (F) Capillary-like network formation by iPSC-ECs from HCs and TKI-treated patients after vehicle or sunitinib exposure; right, quantification of the number of tubes [HCs, $n = 15$ samples (5 patients \times 3 replicates); TKI-treated, $n = 84$ samples (28 patients \times 3 replicates)]. (G) NO production by iPSC-ECs from HCs and TKI-treated patients after vehicle or sunitinib exposure in response to acetylcholine [HCs, $n = 10$ samples (5 patients \times 2 replicates); TKI-treated, $n = 56$ samples (28 patients \times 2 replicates)]. ns, not significant. (H) Hierarchical clustering of bulk RNA-seq data showing DEGs in iPSC-ECs after vehicle or sunitinib exposure. (I) GO enrichment analysis of DEGs highlighting pathways associated with shear stress and mechanical stimuli. (J) Volcano plot of DEGs showing down-regulation of EC markers after sunitinib exposure [false discovery rate (FDR) < 0.05]. (K) Hierarchical clustering of mechanotransduction-associated DEGs in iPSC-ECs exposed to vehicle or sunitinib. [(B) and (D)] P values were calculated using the two-tailed, paired Student's t test. Data are presented as the means \pm SD. [(F) and (G)] P values were calculated using a one-way ANOVA with Bonferroni correction. Data are presented as the means \pm SEM. P values: * $P < 0.05$ and **** $P < 0.0001$. [(E) and (F)] Scale bars, 100 μm.

and NOS3 (fig. S5B) along with reduced angiogenic capacity (fig. S5C) and NO production (fig. S5D). Moreover, patient BECs displayed decreased expression of mechanotransduction-associated genes, including HAS2, TRPV4, PIEZO1, and PIEZO2 (fig. S5E). Together, these results reinforced our iPSC-EC findings and confirmed that VEGFR-TKI therapy disrupts endothelial mechanotransduction in both primary human ECs and circulating progenitor cells, contributing to endothelial dysfunction in patients who develop hypertension during treatment.

Shear stress fails to restore endothelial function after sunitinib treatment

The endothelium, a diaphanous film of tissue, is continuously exposed to fluid shear stress generated by blood flow, which is sensed through specialized mechanoreceptors that regulate downstream signaling to maintain vascular tone (16). Failure to adapt to shear stress contributes to endothelial damage and cardiovascular dysfunction. On the basis of our earlier findings, we hypothesized that VEGFR-TKIs impair endothelial mechanosensors, reducing the

ability of ECs to align with flow and maintain homeostasis. To test this, we subjected iPSC-ECs from TKI-treated patients to laminar shear stress (~ 15 dynes/cm 2) in the presence or absence of sunitinib (0.1 μ M) (fig. S6A). Vehicle-treated iPSC-ECs aligned with the direction of flow, whereas sunitinib-treated iPSC-ECs failed to align properly, consistent with impaired mechanosensing (fig. S6B) (38). Sunitinib-treated cells also exhibited reduced expression of endothelial markers *PECAM1* and *NOS3* (fig. S6C) and down-regulation of mechanotransduction-associated genes *HAS2*, *TRPV4*, and *PIEZO1* (fig. S6D). Functional assays further confirmed endothelial dysfunction, with sunitinib-treated iPSC-ECs showing diminished tube formation (fig. S6E), reduced NO production in response to acetylcholine (fig. S6F), and impaired acetylated LDL uptake (fig. S6G) compared with vehicle controls. Together, these findings

demonstrated that sunitinib treatment impaired endothelial mechanosensing and shear stress–induced alignment, leading to endothelial dysfunction.

Sunitinib induces hypertension and disrupts endothelial mechanotransduction in mice

Hypertension is the most common cardiovascular side effect of VEGFR-TKIs, with nearly all patients undergoing treatment exhibiting elevated blood pressure (39, 40). Consistent with our patient observations, we next tested whether sunitinib impairs vascular function in vivo using a mouse model. C57BL/6J mice were administered sunitinib daily (40 mg/kg, oral gavage) for 3 weeks, a regimen known to achieve plasma concentrations similar to those observed in human patients with cancer (Fig. 2A) (41–43). Consistent with earlier studies

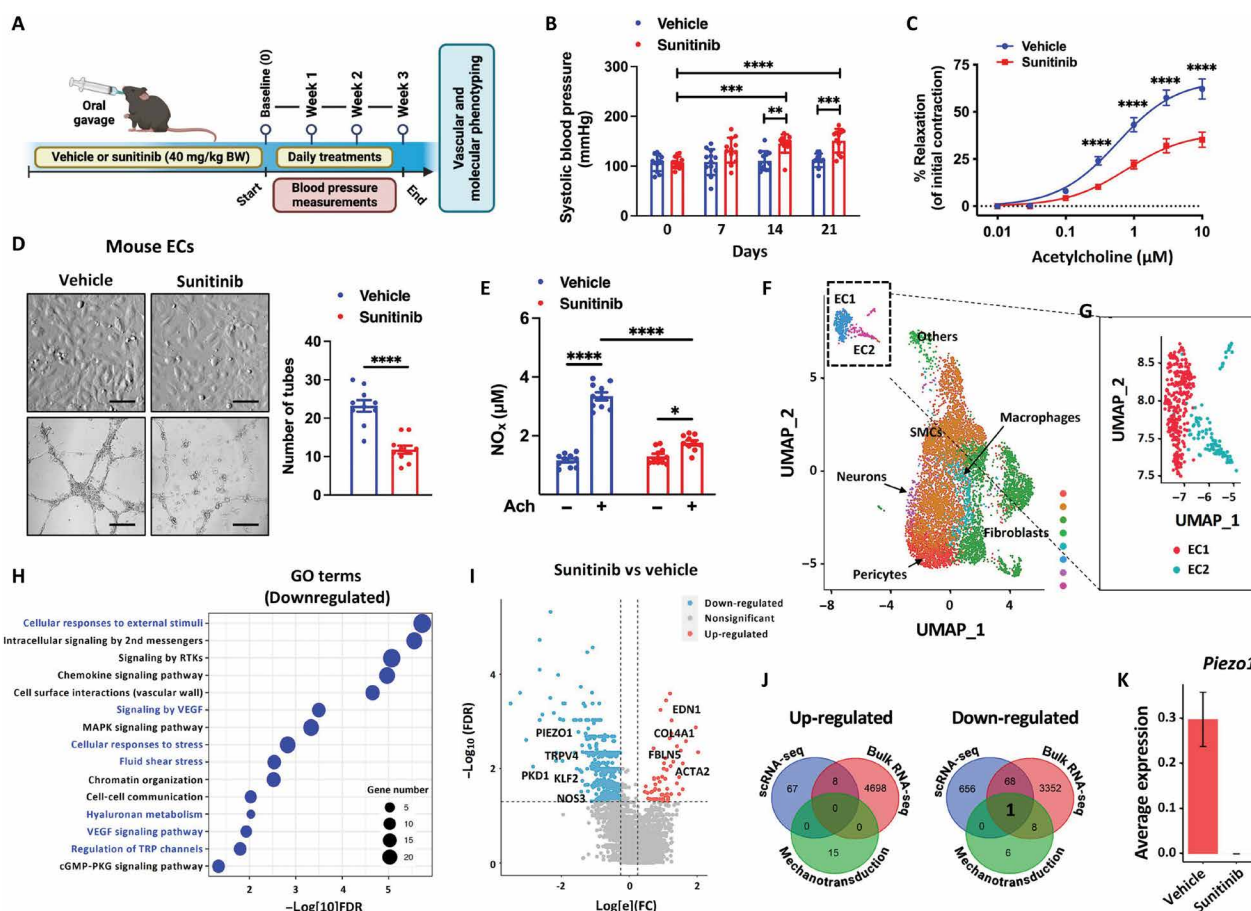


Fig. 2. Sunitinib induces hypertension and disrupts endothelial mechanotransduction in mice. (A) Experimental workflow showing sunitinib treatment in mice and vascular function assessment. Schematic created using BioRender. BW, body weight. (B) Systolic blood pressure in vehicle- and sunitinib-treated mice over 21 days ($n = 12$ mice per group). (C) Percent relaxation of mesenteric arteries in response to acetylcholine, showing impaired vasoactivity in sunitinib-treated mice ($n = 3$ arteries; three segments per artery). (D) Bright-field images of ECs isolated from vehicle- and sunitinib-treated mice showing cobblestone morphology (upper) and capillary-like network formation (lower); right, quantification of the number of tubes [$n = 10$ samples (5 mice \times 2 replicates) per group]. Scale bars, 50 μ m. (E) NO production by ECs isolated from vehicle- and sunitinib-treated mice in response to acetylcholine [$n = 10$ samples (5 mice \times 2 replicates) per group]. (F) UMAP clustering of scRNA-seq profiles from mouse arterial tissues showing major cell populations ($n = 3$ mice pooled per group). (G) UMAP showing two endothelial clusters enriched in sunitinib-treated mice. (H) GO enrichment analysis of DEGs showing down-regulation of endothelial and shear stress–responsive pathways in sunitinib-treated arteries. (I) Volcano plot of endothelial DEGs showing down-regulation of mechanotransduction-associated genes and up-regulation of fibrosis markers. (J) Venn diagram showing overlapping DEGs between human iPSC-EC bulk RNA-seq and mouse arterial scRNA-seq after sunitinib exposure. (K) Piezo1 gene expression in ECs isolated from vehicle- and sunitinib-treated mice. [(B) and (E)] P values were calculated using a one-way ANOVA with Bonferroni correction. Data are presented as the means \pm SD. (C) P values were calculated using a two-way ANOVA with Bonferroni correction. Data are presented as the means \pm SEM. P values: * $P < 0.05$, ** $P < 0.01$, *** $P < 0.001$, and **** $P < 0.0001$.

(29, 44), sunitinib-treated mice developed hypertension within 2 weeks, with increases in both systolic and diastolic pressures compared with vehicle-treated controls (systolic blood pressure: 111 ± 3.9 mmHg vehicle versus 151 ± 6.9 mmHg sunitinib; diastolic blood pressure: 75 ± 5.3 mmHg vehicle versus 109 ± 5.8 mmHg sunitinib) (Fig. 2B and fig. S7A). Heart rate was unchanged between groups (fig. S7B), suggesting that hypertension was primarily driven by altered vascular tone. To assess vascular reactivity, we harvested mesenteric arteries and analyzed them using a wire myograph, which quantifies smooth muscle contraction and relaxation in response to endothelial NO release (45). Although contractile responses to agonists and antagonists were comparable across groups (fig. S7, C and D), arteries from sunitinib-treated mice exhibited impaired acetylcholine-mediated relaxation (Fig. 2C). ECs isolated from these mice further demonstrated reduced tube formation (Fig. 2D) and diminished NO production (Fig. 2E), consistent with endothelial dysfunction.

To explore the underlying transcriptional changes, we performed single-cell RNA-seq (scRNA-seq) on arterial tissues from vehicle- and sunitinib-treated mice. After stringent quality control and filtering, the cells were analyzed for conserved genes and clustered on the basis of similar gene expression profiles. Seven distinct cell clusters were identified, including ECs, SMCs, fibroblasts, pericytes, macrophages, and neurons (Fig. 2F and fig. S7E). Two EC-specific clusters (EC1 and EC2) emerged, with EC2 showing markedly reduced endothelial gene expression (Fig. 2G). Differential expression analysis across EC clusters revealed changes between vehicle- and sunitinib-treated groups (fig. S7F). When projected onto a unified uniform manifold approximation and projection (UMAP), arterial tissue from sunitinib-treated mice was enriched in the EC2 cluster (fig. S7G) and showed down-regulation of endothelial genes, including *Nos3* and *Klf2* (fig. S7H). GO term analysis showed up-regulation of extracellular matrix (ECM) organization and collagen formation pathways, suggestive of fibrosis (fig. S7I), and down-regulation of shear stress, VEGF signaling, and mechanotransduction pathways (Fig. 2H). Consistent with our iPSC-EC findings, sunitinib-treated mice also demonstrated reduced expression of mechanosensors, including *Piezo1*, *Trpv4*, and *Pkd1* (Fig. 2I).

Given that sunitinib-treated iPSC-ECs and mice both exhibited down-regulation of mechanotransduction genes, we sought to identify the most critical driver of dysfunction. For this, we integrated DEGs from iPSC-EC bulk RNA-seq with mouse arterial scRNA-seq. Venn analysis identified *PIEZO1* as the only mechanotransduction gene consistently down-regulated across datasets (Fig. 2J). Direct comparison confirmed reduction of *Piezo1* expression in ECs from sunitinib-treated mice (Fig. 2K). Collectively, these findings demonstrated that sunitinib induces hypertension and endothelial dysfunction *in vivo*, mediated at least in part through disruption of mechanotransduction pathways and down-regulation of the mechanosensor *PIEZO1*.

Modulation of *PIEZO1* prevents sunitinib-induced endothelial dysfunction

PIEZO1, a mechanically activated ion channel, is central to endothelial mechanotransduction by sensing shear stress from blood flow (16). By mediating calcium influx, *PIEZO1* maintains vascular homeostasis, and disruption of this ion channel has been associated with hypertension, vascular remodeling, cardiac fibrosis, and hypertrophy (46, 47). To test the role of *PIEZO1* in sunitinib-induced EC dysfunction, we first performed a genetic loss-of-function approach. *PIEZO1* knockdown in iPSC-ECs using short hairpin RNA abrogated flow-mediated alignment

in both vehicle- and sunitinib-treated cells (fig. S8, A and B). *PIEZO1* knockdown in iPSC-ECs showed reduced expression of *PIEZO1* and *PECAM1* (fig. S8C) and exhibited impaired functionality, including defective tube formation (fig. S8D), diminished NO production (fig. S8E), and reduced acetylated LDL uptake (fig. S8F). These deficits occurred in both vehicle- and sunitinib-treated groups, underscoring the essential role of *PIEZO1* in maintaining baseline EC function.

We next asked whether restoring *PIEZO1* expression was sufficient to rescue EC dysfunction induced by VEGFR-TKI treatment. To do so, we established a doxycycline-inducible *PIEZO1* overexpression system in iPSCs using the piggyBac Tet-On platform (Fig. 3, A and B). Stably transfected iPSCs were differentiated into iPSC-ECs without doxycycline, permitting endogenous *PIEZO1* expression. At the baseline, these iPSC-ECs displayed characteristic cobblestone morphology, intact tube formation, and preserved NO production (Fig. 3, C to E). Exposure to sunitinib induced marked dysfunction, with loss of tube formation and reduced NO release. Notably, after sunitinib washout and doxycycline-mediated *PIEZO1* induction, endothelial function was restored, with tube formation and NO production returning to near-baseline levels (Fig. 3, D and E). To evaluate whether *PIEZO1* induction conferred resilience to further stress, we reexposed doxycycline-induced iPSC-ECs to sunitinib. Although modest impairments were noted, endothelial function remained higher than during the initial challenge, suggesting partial protection against repeated injury.

Bulk RNA-seq across sequential conditions (baseline, sunitinib exposure, doxycycline rescue, and sunitinib reexposure) revealed distinct transcriptional shifts (Fig. 3F). GO analysis confirmed that sunitinib down-regulated pathways involved in mechanotransduction, including responses to mechanical stimuli and fluid shear stress, focal adhesion signaling, and vascular SMC contraction, and these pathways were restored after *PIEZO1* induction (Fig. 3G). At the gene level, sunitinib suppressed endothelial markers (*PECAM1*, *CDH5*, and *NOS3*) and mechanosensors (*PIEZO1* and *TRPV4*), whereas doxycycline-mediated *PIEZO1* overexpression reversed this pattern. *PIEZO1*-induced iPSC-ECs maintained endothelial gene expression even after reexposure to sunitinib, demonstrating transcriptional resilience (Fig. 3, H and I). Collectively, these findings established *PIEZO1* as a master regulator of endothelial homeostasis. Both knockdown and inducible overexpression experiments confirmed its causal role in mediating the endothelial response to sunitinib and highlighted *PIEZO1* as a potential therapeutic target to mitigate TKI-induced endothelial toxicity.

Yoda1 restores sunitinib-induced endothelial dysfunction

To evaluate whether pharmacological activation of *PIEZO1* could rescue EC function after VEGFR-TKI exposure, iPSC-ECs were simultaneously treated with sunitinib (0.1 μ M) and *Yoda1* (1 μ M), a selective *PIEZO1* agonist (48), under flow-mediated conditions (Fig. 4A). As expected, vehicle-treated iPSC-ECs aligned with the direction of flow, whereas sunitinib-treated iPSC-ECs failed to do so (Fig. 4B). Cotreatment with *Yoda1* prevented this misalignment, restoring flow-induced alignment, consistent with a prior report of *PIEZO1*-dependent mechanosensing (49). *Yoda1* treatment also improved EC function. Under flow, sunitinib-treated iPSC-ECs displayed impaired tube formation, reduced NO production, and diminished acetylated LDL uptake, all of which were rescued by *Yoda1* (Fig. 4, C to E). In contrast, vehicle-treated iPSC-ECs exhibited no significant changes in function upon *Yoda1* treatment.

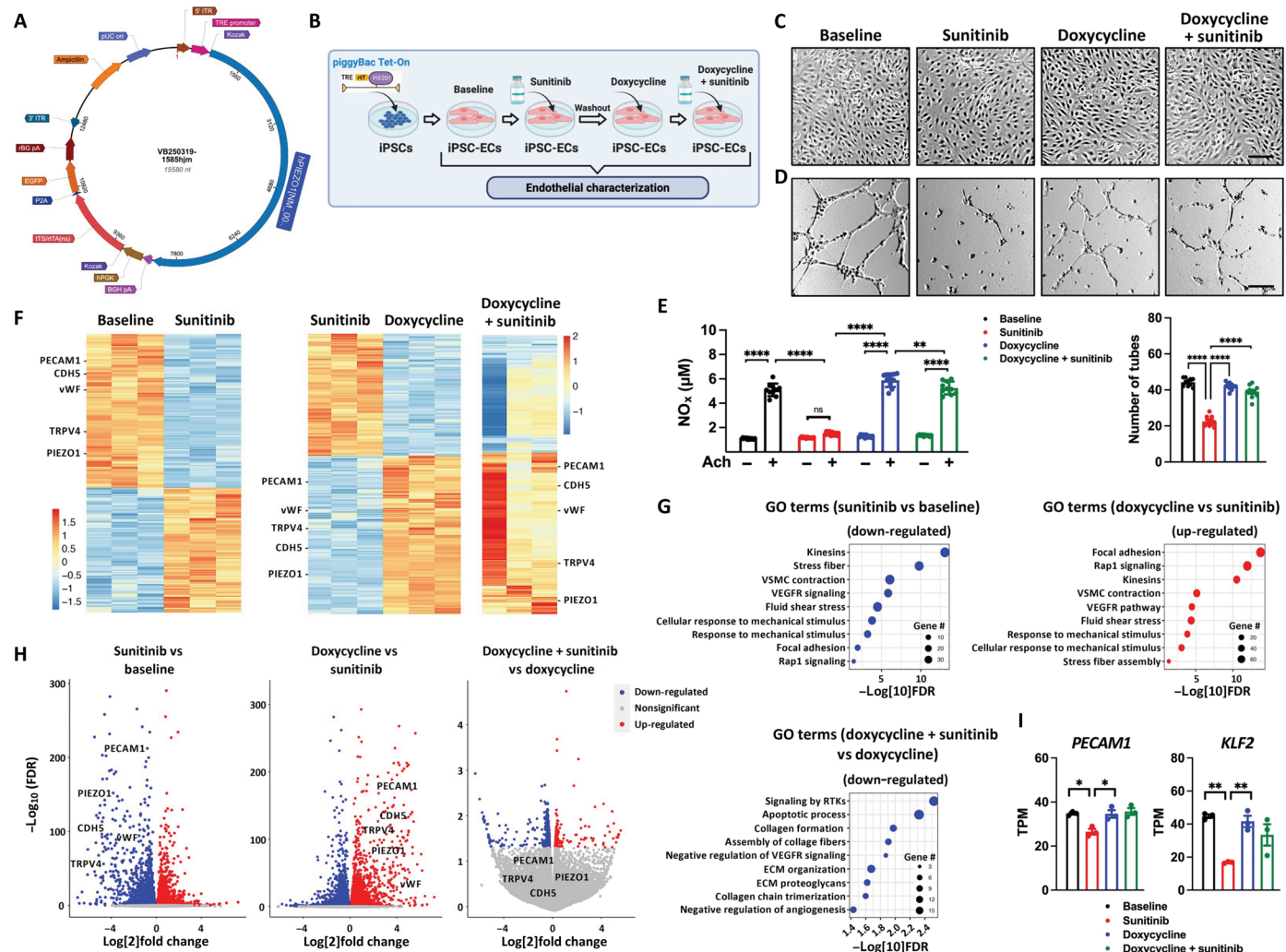


Fig. 3. Inducible overexpression of PIEZO1 restores endothelial function and transcriptomic identity under sunitinib stress. (A) Schematic of the piggyBac Tet-On inducible PIEZO1 overexpression system. Schematic created using BioRender. (B) Experimental timeline showing differentiation of inducible PIEZO1 iPSCs into iPSC-ECs, followed by sequential exposure to sunitinib, doxycycline-mediated PIEZO1 induction, and sunitinib reexposure. Schematic created using BioRender. (C) Bright-field images of iPSC-ECs showing cobblestone morphology at the baseline, after sunitinib exposure, after doxycycline rescue, and after sunitinib reexposure. (D) Capillary-like network formation at the baseline, after sunitinib exposure, after doxycycline rescue, and after sunitinib reexposure; bottom, quantification of the number of tubes ($n = 10$ iPSC-EC samples per condition). (E) NO production by iPSC-ECs in response to acetylcholine at the baseline, after sunitinib exposure, after doxycycline rescue, and after sunitinib reexposure ($n = 10$ samples per condition). (F) Hierarchical clustering of bulk RNA-seq data from iPSC-ECs across sequential treatment conditions. (G) GO enrichment analysis of DEGs from bulk RNA-seq. (H) Volcano plots of DEGs comparing sunitinib versus baseline, doxycycline versus sunitinib, and sunitinib reexposure versus doxycycline, highlighting endothelial and mechanosensitive genes (PECAM1, CDH5, PIEZO1, and TRPV4). (I) Transcript per million (TPM) values for PECAM1 and KLF2 across treatment conditions ($n = 3$ samples per condition). [(D) and (I)] P values were calculated using a one-way ANOVA with Bonferroni correction. Data are presented as the means \pm SEM. (E) P values were calculated using a one-way ANOVA with Bonferroni correction. Data are presented as the means \pm SD. P values: * $P < 0.05$, ** $P < 0.01$, and *** $P < 0.0001$. [(C) and (D)] Scale bars, 100 μ m.

To test whether Yoda1 restored global EC transcriptional programs, we performed bulk RNA-seq on iPSC-ECs exposed to sunitinib with or without Yoda1. Hierarchical clustering revealed distinct transcriptional profiles between groups (Fig. 4F). GO enrichment analysis showed that sunitinib suppressed pathways related to mechanotransduction, including fluid shear stress, focal adhesion, and VEGF signaling, whereas Yoda1 cotreatment reactivated these programs (Fig. 4G). At the gene level, Yoda1 reversed the down-regulation of canonical endothelial and mechanosensitive genes, including PECAM1, NOS3, KLF2, PIEZO1, and TRPV4,

caused by sunitinib (Fig. 4, H and I). Together, these findings demonstrated that pharmacological activation of PIEZO1 using Yoda1 restored both functional and transcriptional features of endothelial identity under VEGFR-TKI stress, reinforcing PIEZO1 as a critical regulator of mechanosensing and vascular integrity.

Yoda1 prevents sunitinib-induced hypertension and restores mechanotransduction in mice

Piezo1 knockout mice develop vascular dysfunction and hypertension (46), and endothelial-specific deletion of *Piezo1* reduces NOS3

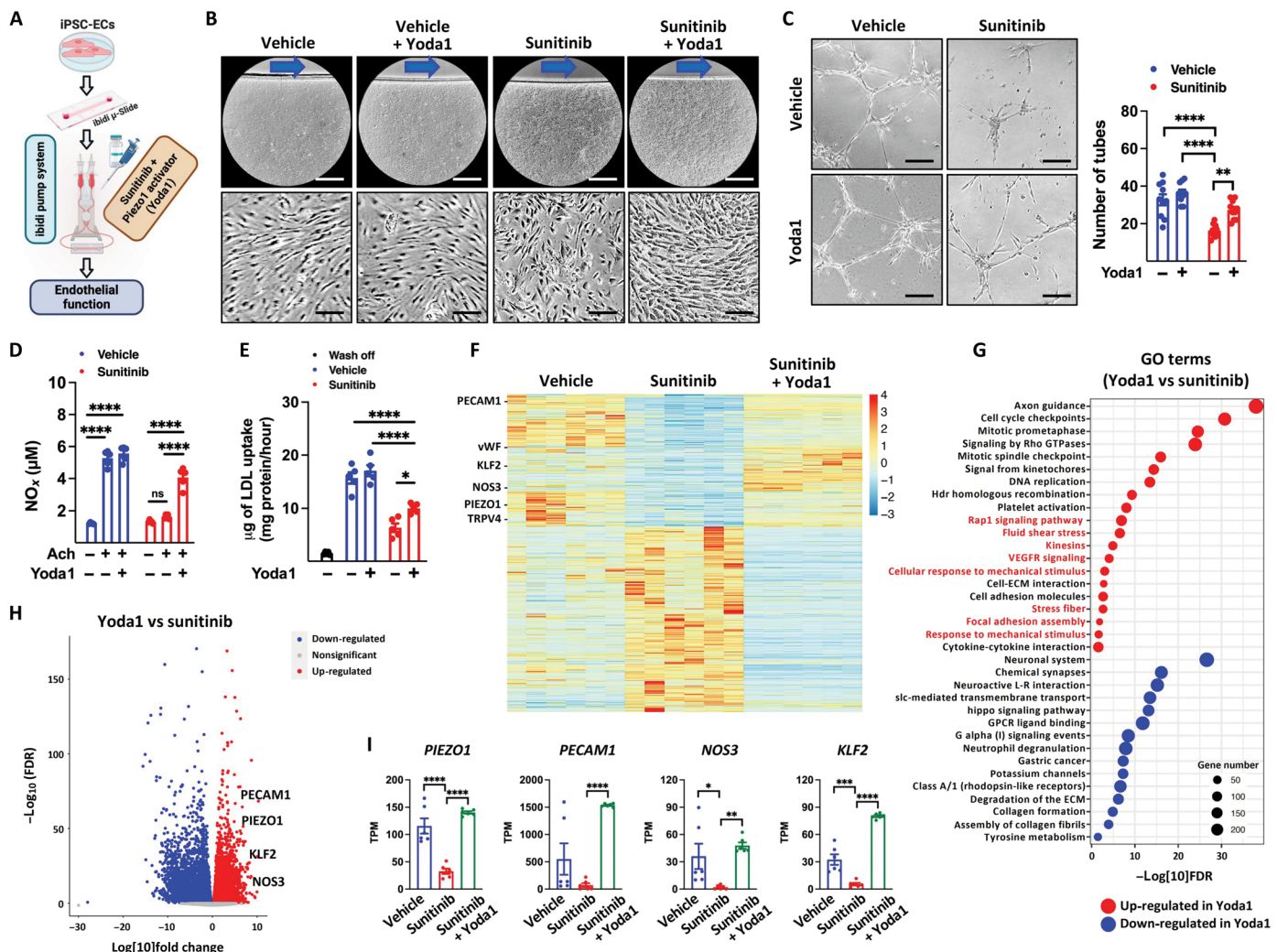


Fig. 4. Activation of PIEZO1 prevents sunitinib-induced endothelial dysfunction. (A) Experimental workflow showing application of flow-mediated shear stress in the presence or absence of sunitinib and Yoda1. Schematic created using BioRender. (B) Bright-field images of iPSC-ECs treated with vehicle or sunitinib under shear stress with or without Yoda1; arrows indicate flow direction. Scale bars, 50 μ m. (C) Capillary-like network formation by iPSC-ECs treated with vehicle, sunitinib, or sunitinib + Yoda1; right, quantification of the number of tubes ($n = 10$ iPSC-EC samples per condition). (D) NO production by iPSC-ECs in response to acetylcholine under vehicle, sunitinib, or sunitinib + Yoda1 conditions ($n = 5$ samples per condition). (E) Ac-LDL uptake by iPSC-ECs treated with vehicle, sunitinib, or sunitinib + Yoda1 ($n = 5$ samples per condition). (F) Hierarchical clustering of bulk RNA-seq data from iPSC-ECs treated with vehicle, sunitinib, and sunitinib + Yoda1. (G) GO enrichment analysis of DEGs between sunitinib and sunitinib + Yoda1 conditions. (H) Volcano plot of DEGs comparing sunitinib- and sunitinib + Yoda1-treated iPSC-ECs. (I) TPM values for *PIEZO1*, *PECAM1*, *NOS3*, and *KLF2* across treatment conditions ($n = 6$ samples per condition). [(C) to (E) and (I)] P values were calculated using a one-way ANOVA with Bonferroni correction. Data are presented as the means \pm SEM. P values: * $P < 0.05$, ** $P < 0.01$, *** $P < 0.001$, and **** $P < 0.0001$. [(B) and (C)] Scale bars, 50 μ m.

phosphorylation and NO production (46). Because sunitinib treatment resulted in *Piezo1* haploinsufficiency and hypertension, we hypothesized that pharmacological activation of *Piezo1* with Yoda1 could mitigate these effects. Mice were cotreated daily with Yoda1 (5 mg/kg, intraperitoneally) and sunitinib (40 mg/kg, by oral gavage) for 3 weeks, and blood pressure was monitored weekly (Fig. 5A). As expected, heart rate remained unchanged across groups (fig. S9A). Sunitinib alone caused a progressive increase in systolic and diastolic blood pressure, whereas coadministration of Yoda1 prevented hypertension (Fig. 5B and fig. S9B). Wire myograph analysis of mesenteric arteries showed that Yoda1-treated mice exhibited improved acetylcholine-induced relaxation compared with sunitinib-treated mice, whereas isometric contractile responses remained comparable

across groups (Fig. 5C and fig. S9, C and D). ECs isolated from vascular tissues of Yoda1 + sunitinib–treated mice retained the ability to form vascular networks and produce NO, in contrast with ECs from sunitinib-only mice (Fig. 5, D and E). These findings demonstrated that Yoda1 preserved endothelial function and prevented sunitinib-induced hypertension.

To investigate underlying mechanisms, we performed scRNA-seq on arterial tissues collected from Yoda1-treated mice and compared their RNA profiles with those of sunitinib-treated mice. UMAP clustering of Yoda1-treated samples identified ECs, SMCs, fibroblasts, and neurons, which separated distinctly from sunitinib-treated samples (Fig. 5F and fig. S9E). The aberrant endothelial subclusters observed with sunitinib were absent in Yoda1-treated arteries (fig. S9F).

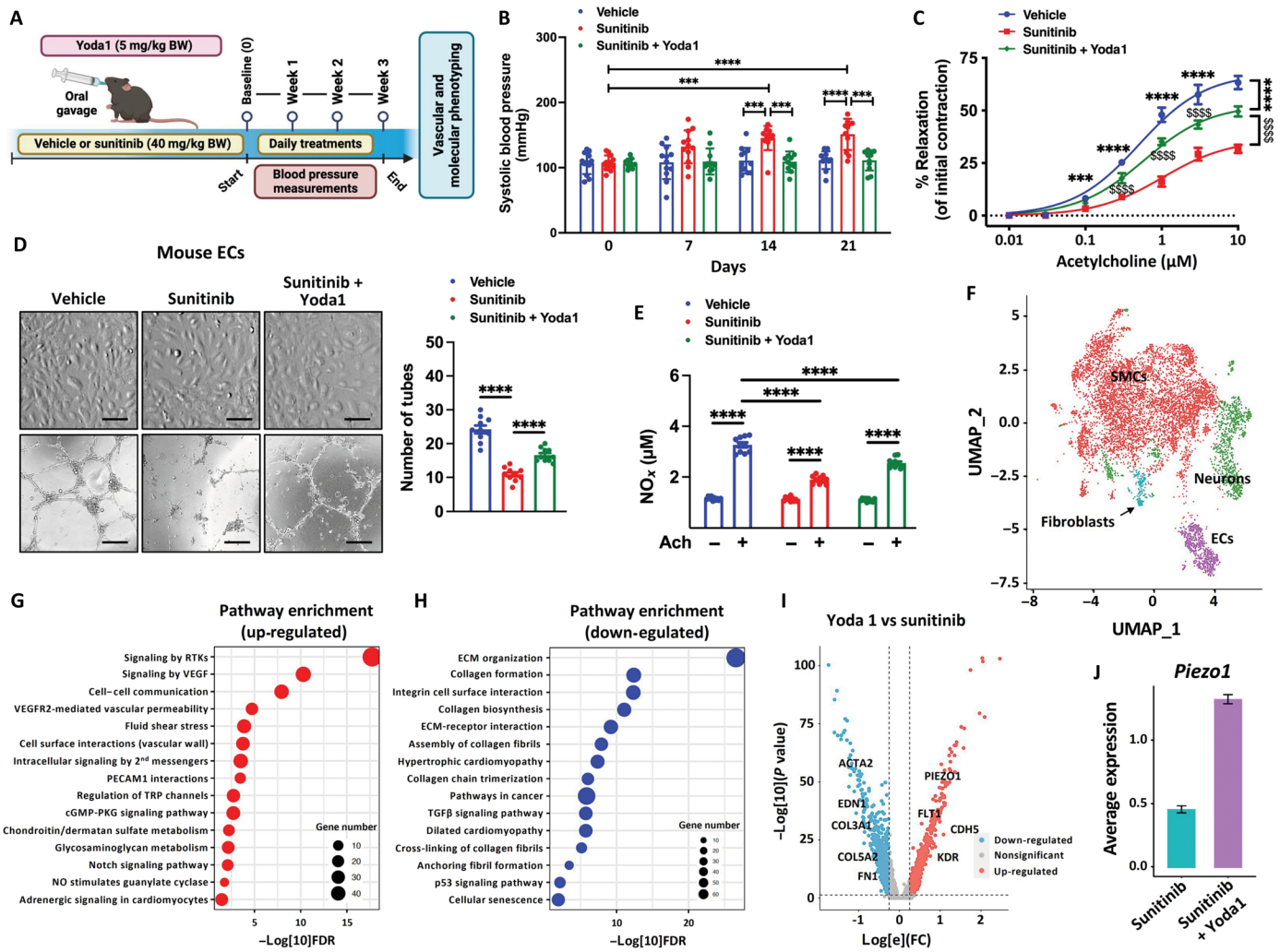


Fig. 5. Yoda1 prevents sunitinib-induced hypertension and restores mechanotransduction in mice. (A) Experimental workflow showing vehicle, sunitinib, or sunitinib + Yoda1 treatment in mice followed by vascular assessments. Schematic created using BioRender. (B) Systolic blood pressure in mice across 21 days of treatment ($n = 11$ or 12 mice per group). (C) Percent relaxation of mesenteric arteries in response to acetylcholine in each treatment group ($n = 3$ arteries per group; three segments per artery). (D) Bright-field images of ECs isolated from each treatment group showing cobblestone morphology (upper) and capillary-like network formation (lower); right, quantification of the number of tubes [$n = 10$ samples (5 mice \times 2 replicates) per group]. Scale bars, 50 μ m. (E) NO production by ECs isolated from vehicle-, sunitinib-, and sunitinib + Yoda1-treated mice after acetylcholine stimulation [$n = 10$ samples (5 mice \times 2 replicates) per group]. (F) UMAP of scRNA-seq from mouse arterial tissues showing transcriptional clusters across treatment groups ($n = 3$ pooled mice per group). (G) GO enrichment analysis of DEGs from scRNA-seq comparing sunitinib and sunitinib + Yoda1 groups. (H) GO enrichment analysis of DEGs for ECM and collagen-associated pathways. (I) Volcano plot of DEGs in endothelial clusters from sunitinib and sunitinib + Yoda1 groups. (J) Piezo1 expression in ECs isolated from each treatment group ($n = 3$ pooled mice per group). (B) P values were calculated using a one-way ANOVA with Bonferroni correction. Data are presented as the means \pm SD. (C) P values were calculated using a two-way ANOVA with Bonferroni correction. Data are presented as the means \pm SEM. P values: *** $P < 0.001$, **** $P < 0.0001$, and \$\$\$\$ $P < 0.0001$.

Differential expression analysis revealed that Yoda1 restored the expression of endothelial markers (*Flt1* and *Kdr*) and suppressed mesenchymal markers (*Acta2* and *Tagln*) (fig. S9G). GO analysis of DEGs highlighted the enrichment of mechanotransduction pathways, including fluid shear stress responses, TRP (transient receptor potential) channel regulation, and *Pecam1* interactions in Yoda1-treated samples (Fig. 5G). Conversely, fibrosis-related pathways, such as collagen biosynthesis, ECM organization, and myofibroblast activation, were down-regulated (Fig. 5H). At the gene level, Yoda1 increased the expression of mechanotransduction-associated genes (*Piezo1*, *Flt1*, and *Cdh5*) and reduced fibrogenesis-associated genes (*Col3a1*,

Fn1, and *Acta2*) (Fig. 5, I and J). Collectively, these results established that pharmacological activation of PIEZO1 by Yoda1 restored endothelial mechanotransduction, suppressed mesenchymal transition, and prevented vascular dysfunction and hypertension induced by sunitinib.

Yoda1 prevents sunitinib-induced cardiotoxicity

TKIs such as sunitinib are associated with cardiotoxicities, including reduced left ventricular ejection fraction (LVEF), myocardial infarction, and heart failure. Retrospective studies report that 7 to 15% of patients treated with sunitinib develop symptomatic class

III/IV heart failure (14, 23, 50). Although sunitinib-induced cardiomyopathy is often described as transient (20, 51), the mechanisms contributing to long-term cardiac dysfunction remain poorly understood. Most patients with class III LVEF dysfunction also develop grade 3 hypertension, which typically manifests earlier than heart failure and may contribute to its progression (52). In our clinical cohort, 6 of 28 patients exhibited reduced LVEF (Fig. 6, A and B). To model long-term consequences, we assessed cardiac function in mice 12 weeks after discontinuing a 3-week course of sunitinib. LVEF and fractional shortening (FS) were also evaluated in mice cotreated with sunitinib and Yoda1 (Fig. 6C). During acute treatment,

sunitinib induced progressive hypertension but no immediate changes in cardiac function. By week 15, however, previously treated mice exhibited reduced LVEF and FS (Fig. 6, D to F). In contrast, cotreatment with Yoda1 preserved normal cardiac function, indicating a protective effect.

To explore underlying mechanisms, we performed integrative single-cell multiomics [single-nucleus RNA-seq and snRNA-seq + single-nucleus assay for transposase-accessible chromatin sequencing (snATAC-seq)] on cardiac tissues from mice treated with vehicle, sunitinib, or sunitinib + Yoda1 (Fig. 6G). UMAP clustering identified seven major populations, including CMs, ECs, fibroblasts,

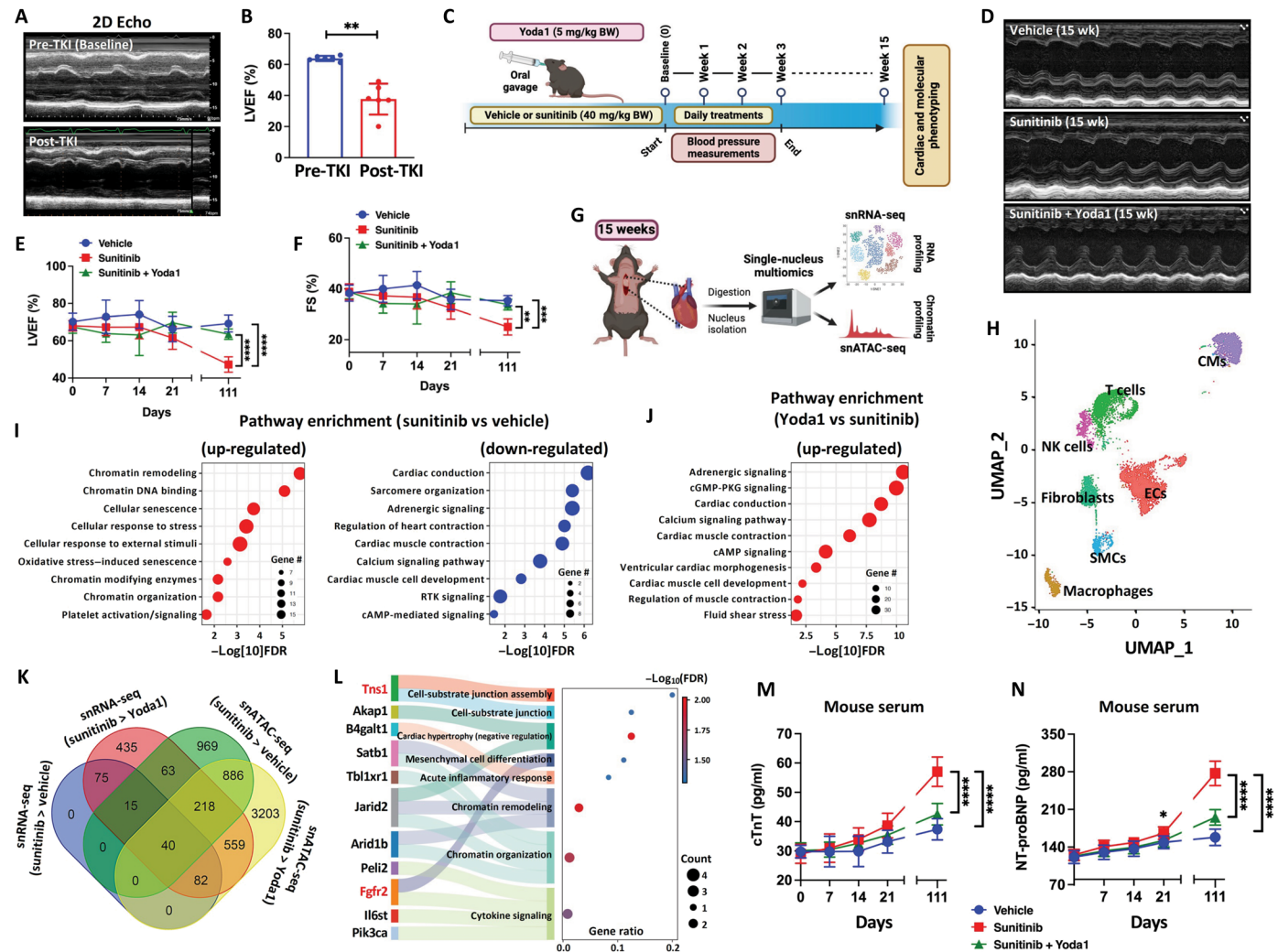


Fig. 6. Yoda1 prevents sunitinib-induced cardiototoxicity. (A) Representative cine loop M-mode echocardiograms from patients treated with TKIs at the baseline and after treatment. (B) LVEF (%) in patients before and after TKI treatment ($n = 6$ patients). (C) Experimental workflow for long-term evaluation of cardiac function in mice treated with vehicle, sunitinib, or sunitinib + Yoda1. Schematic created using BioRender. (D) Representative M-mode echocardiographic images of mouse left ventricle at week 15. (E and F) LVEF (E) and FS (F) in mice from each treatment group ($n = 8$ to 10 mice per group). (G) Workflow for nucleus isolation and single-nucleus multiome (snRNA-seq + snATAC-seq) profiling from mouse heart tissues. Schematic created using BioRender. (H) UMAP of nuclei showing transcriptional clusters across treatment groups. (I) Pathway enrichment analysis of DEGs from snRNA-seq comparing vehicle and sunitinib groups. (J) Pathway enrichment analysis of DEGs from snRNA-seq comparing vehicle and sunitinib + Yoda1 groups. (K) Venn diagram showing overlapping DEGs between snRNA-seq and snATAC-seq datasets across treatment groups. (L) Sankey plot illustrating DEGs associated with chromatin remodeling, cardiac hypertrophy, mesenchymal stem cell differentiation, and cytokine signaling pathways identified across treatment groups. (M and N) Serum levels of (M) cTnT and (N) NT-proBNP measured by ELISA in mice from each treatment group [$n = 16$ samples (8 mice \times 2 replicates) per group]. (B) P values were calculated using the two-tailed, paired Student's *t* test. Data are presented as the means \pm SD. [(E), (F), (M), and (N)] P values were calculated using a one-way ANOVA with Bonferroni correction. Data are presented as the means \pm SD. P values: * $P < 0.05$, ** $P < 0.01$, *** $P < 0.001$, and **** $P < 0.0001$.

SMCs, T cells, natural killer cells, and macrophages (Fig. 6H and fig. S10, A and B). GO enrichment analysis of CMs from sunitinib-treated mice revealed up-regulation of chromatin modification and senescence pathways, with down-regulation of cardiac contraction, calcium handling, and adrenergic signaling (Fig. 6I). These functional pathways remained preserved in Yoda1-treated mice (Fig. 6J), alongside enhanced expression of fluid shear stress–responsive genes. To identify regulatory drivers of long-term sunitinib effects, we integrated snRNA-seq and snATAC-seq datasets across treatment groups, revealing 40 candidate genes altered by sunitinib and reversed by Yoda1 (Fig. 6K and fig. S10C). A Sankey plot highlighted 11 genes linked to chromatin remodeling, cardiac hypertrophy, mesenchymal stem cell differentiation, and cytokine signaling that were suppressed by Yoda1 (Fig. 6L). Chromatin accessibility analysis further identified fibroblast growth factor receptor 2 (*Fgfr2*), a receptor tyrosine kinase linked to osteogenesis (53) and epithelial-mesenchymal transition (54), and tensin 1 (*Tns1*), a regulator of myofibroblast differentiation and ECM formation, as key loci with increased accessibility in sunitinib-exposed CMs (fig. S10, D and E). Yoda1 treatment mitigated accessibility changes at both loci, consistent with corresponding gene expression profiles (fig. S10, F and G).

To assess whether these molecular signatures translated into functional outcomes, we measured circulating cardiac stress biomarkers. Serum cardiac troponin T (cTnT) and N-terminal pro-brain natriuretic peptide (NT-proBNP), established markers of myocardial injury and ventricular strain, were elevated in sunitinib-treated mice compared with vehicle controls (Fig. 6, M and N). Cotreatment with Yoda1 normalized both markers to near baseline, paralleling the restoration of cardiac gene expression and chromatin accessibility observed in our single-nucleus analyses. These findings demonstrated that Yoda1 preserved CM identity and function at transcriptional, epigenomic, and physiological levels. Furthermore, the reversal of sunitinib-induced chromatin remodeling, together with normalization of circulating biomarkers, suggested that *PIEZO1* activation not only prevented CM dysfunction but also mitigated downstream fibrotic remodeling. This integrative evidence underscored the therapeutic potential of *PIEZO1* activation in preserving long-term cardiovascular health during chemotherapy.

Sunitinib-induced impairment of endothelial mechanotransduction drives CM dysfunction in human cardiac organoids

To determine whether sunitinib-induced CM dysfunction arises from disrupted endothelial mechanotransduction, we used engineered three-dimensional human cardiac organoids (COs) (55, 56) to model EC-CM cross-talk implicated in cardiotoxicity. Using a “minus-one” strategy, COs were fabricated from iPSC-ECs and iPSC-CMs or from iPSC-CMs alone and then exposed to vehicle or sunitinib under flow (Fig. 7, A and B). EC function, assessed by NO production, was impaired in sunitinib-treated COs containing both iPSC-ECs and iPSC-CMs but not in iPSC-CM–only organoids. Cotreatment with Yoda1 restored NO release, indicating the rescue of the endothelial phenotype (Fig. 7C). Contractile performance was evaluated using high-speed video microscopy with motion vector analysis (57), which generated contraction and relaxation traces for each treatment group (fig. S11A). Although spontaneous beating rates were unchanged (fig. S11B), sunitinib-treated COs containing both iPSC-ECs and iPSC-CMs exhibited impaired contraction and relaxation velocities, which were fully restored by Yoda1 (Fig. 7, D

and E, and fig. S12). As previously reported (24), sunitinib at this concentration did not impair contractility in iPSC-CM–only COs, underscoring the critical role of ECs in CM dysfunction. Calcium imaging further revealed elevated diastolic Ca^{2+} , reduced Ca^{2+} transient amplitude, and slowed kinetics in sunitinib-treated COs containing both iPSC-ECs and iPSC-CMs, all of which were reversed by Yoda1 (Fig. 7, F and G, and figs. S11, C and D, and S12). To corroborate these findings, COs were generated using iPSC-ECs pretreated with vehicle, sunitinib, or sunitinib + Yoda1 (fig. S13, A and B). Organoids containing sunitinib-pretreated ECs exhibited impaired contractility and reduced *MYH6* and *MYH7* expression, both of which were restored when iPSC-ECs were co-pretreated with Yoda1 (fig. S13, C to E).

We next examined global gene expression in COs after sunitinib and Yoda1 treatment. Principal components analysis of RNA-seq data revealed distinct clustering of treatment groups (fig. S13F), with DEGs between vehicle-, sunitinib-, and sunitinib + Yoda1-treated organoids (Fig. 7H). In COs containing iPSC-ECs and iPSC-CMs, sunitinib up-regulated chromatin remodeling and ECM organization pathways and down-regulated cardiac contraction, calcium signaling, and adrenergic pathways (Fig. 7I). These effects were reversed by Yoda1, whereas iPSC-CM–only COs showed no significant pathway changes (fig. S13G). At the gene level, sunitinib suppressed endothelial markers (*PECAM1*, *CDH5*, and *NOS3*), CM markers (*MYH6* and *MYH7*), calcium-handling genes (*PLN* and *RYR2*), and mechanotransduction genes, including *PIEZO1*, all of which were restored by Yoda1 (Fig. 7, J and K, and fig. S13H). iPSC-CM–only COs displayed no significant transcriptomic changes after sunitinib exposure (fig. S13I). Consistent with these transcriptomic and functional results, sunitinib increased cTnT release in COs containing iPSC-ECs and iPSC-CMs but not in iPSC-CM–only organoids, and this effect was prevented by Yoda1 (Fig. 7L).

To test the causal role of endothelial *PIEZO1*, we used a doxycycline-inducible *PIEZO1* overexpression system in iPSC-ECs. COs were generated by combining wild-type iPSC-CMs with *PIEZO1*-inducible iPSC-ECs, enabling selective modulation of endothelial *PIEZO1*. Organoids were assessed at the baseline, after sunitinib exposure, and after *PIEZO1* induction by doxycycline (fig. S14, A and B). At the baseline, COs exhibited robust NO release, which was diminished by sunitinib and restored upon *PIEZO1* induction (fig. S14C), indicating functional rescue of the endothelial compartment within the organoids. CM function was also assessed by analyzing contractile performance and calcium-handling properties of the COs. Although the spontaneous beating rate was unchanged across groups (fig. S14D), contraction and relaxation velocities, impaired in sunitinib-exposed COs, were fully restored by *PIEZO1* overexpression (fig. S14, E and F). Similarly, *PIEZO1* induction rescued sunitinib-induced abnormalities in calcium dynamics, including elevated diastolic Ca^{2+} , reduced transient amplitude, and delayed Ca^{2+} reuptake (fig. S14, G to I). To evaluate the molecular impact of endothelial *PIEZO1* restoration in COs, bulk RNA-seq was conducted, which revealed distinct gene expression changes across conditions (fig. S14J). It confirmed restoration of pathways and genes associated with mechanotransduction (*PIEZO1*), endothelial identity (*PECAM1*), CM contractility (*MYH7*), and calcium handling (*RYR2*) after *PIEZO1* induction (fig. S14, K to N). Consistently, *PIEZO1* induction reduced cTnT release in sunitinib-exposed COs, indicating preserved CM integrity (fig. S14O).

Together, these integrated functional, transcriptomic, and genetic analyses demonstrated that disruption of endothelial mechanotransduction via *PIEZO1* down-regulation drives sunitinib-induced

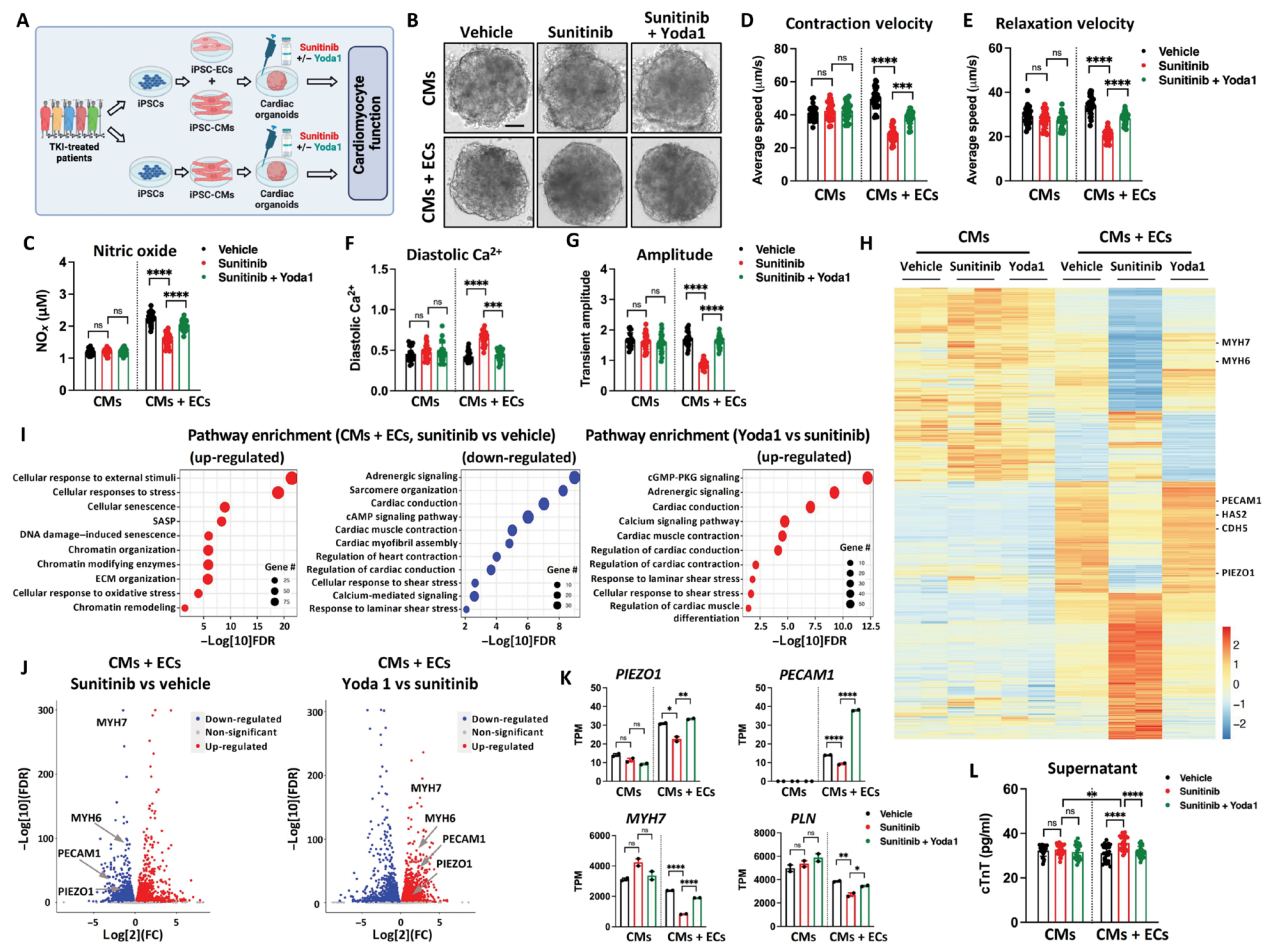


Fig. 7. Sunitinib-induced disruption of endothelial mechanotransduction leads to CM dysfunction in human COs. (A) Experimental workflow for iPSC-derived COs composed of iPSC-CMs alone or iPSC-CMs combined with iPSC-ECs, treated with vehicle, sunitinib, or sunitinib + Yoda1. Schematic created using BioRender. (B) Bright-field images of COs under vehicle, sunitinib, and sunitinib + Yoda1 treatment conditions. Scale bar, 100 μm. (C) NO production in COs composed of iPSC-CMs and iPSC-ECs after vehicle, sunitinib, or sunitinib + Yoda1 treatment [$n = 25$ samples (5 COs × 5 replicates) per group]. (D and E) Contractile parameters of COs composed of iPSC-CMs and iPSC-ECs showing (D) contraction velocity and (E) relaxation velocity across treatment conditions [$n = 25$ samples (5 COs × 5 replicates) per group]. (F and G) Calcium handling metrics in COs composed of iPSC-CMs and iPSC-ECs showing (F) diastolic Ca²⁺ levels and (G) Ca²⁺ transient amplitude [$n = 25$ samples (5 COs × 5 replicates) per group]. (H) Hierarchical clustering of bulk RNA-seq data from COs across vehicle, sunitinib, and sunitinib + Yoda1 treatment conditions. (I) Pathway enrichment analysis of RNA-seq data comparing COs across the three treatment conditions. (J) Volcano plots of DEGs from bulk RNA-seq comparing sunitinib versus vehicle (left) and sunitinib + Yoda1 versus sunitinib (right). Differential expression was determined using linear mixed-effects regression. (K) TPM values for EC markers (PIEZO1 and PECAM1) and CM markers (MYH7 and PLN) across treatment groups ($n = 2$ COs per group). (L) Enzyme-linked immunosorbent assay (ELISA) quantification of cTnT in CO supernatants across treatment conditions [$n = 25$ samples (5 COs × 5 replicates) per group]. [(C) to (G) and (L)] P values were calculated using a one-way ANOVA with Bonferroni correction. Data are presented as the means ± SD. (K) P values were calculated using a one-way ANOVA with Bonferroni correction. Data are presented as the means ± SEM. P values: *P < 0.05, **P < 0.01, ***P < 0.001, and ****P < 0.0001.

cardiotoxicity. Restoration of *PIEZO1*, by pharmacological or genetic means, rescued endothelial function, preserved EC-CM cross-talk, and prevented downstream molecular and functional manifestations of cardiotoxicity. These findings identified *PIEZO1* as a regulator of vascular-cardiac homeostasis and a promising therapeutic target for preventing TKI-induced cardiovascular toxicity.

DISCUSSION

Although TKIs have revolutionized cancer therapy, they are associated with cardiovascular risks (3, 58). Despite their targeted mechanisms and reduced systemic toxicity compared with traditional

chemotherapy, TKIs have been linked to hypertension, heart failure, arrhythmias, and thromboembolic events (6). Among them, VEGFR-TKIs, which block angiogenesis by targeting the VEGFR kinase domain, frequently induce hypertension (9), and growing evidence suggests that they also cause endothelial dysfunction (13). Hypertension incidence varies with the specific inhibitor and cancer type, reaching up to 66% in sunitinib-treated patients with renal cell carcinoma (39) and ranging from 23 to 28% in other contexts (59). Consistent with these reports, patients in our cohort displayed TKI-associated hypertension and impaired endothelial function, as measured by the RHI. Using iPSC-derived ECs, we further demonstrated that sunitinib had the most profound effect on endothelial function,

disrupting key components of the mechanotransduction machinery. In this study, we investigated how VEGFR-TKIs disrupt endothelial mechanotransduction and contribute to cardiac dysfunction.

Animal studies have shown that TKIs induce cardiotoxicity characterized by hypertension, structural changes in CMs, and impaired cardiac function, with proposed mechanisms including mitochondrial injury and ER stress, particularly at higher doses of certain TKIs like sunitinib (15, 29, 44, 60, 61). Our *in vivo* experiments confirmed these observations: Mice treated with sunitinib developed a ~30% increase in systolic blood pressure within 3 weeks, impaired vascular reactivity, and EC dysfunction consistent with our iPSC-EC findings. Single-cell profiling of vascular tissues revealed down-regulation of endothelial and mechanotransduction genes, in agreement with bulk RNA-seq results from iPSC-ECs and prior reports (43, 62). These tissues also showed the enrichment of collagen biosynthesis and ECM organization pathways, consistent with endothelial-to-mesenchymal transition and fibrosis. Integration of vascular single-cell data with iPSC-EC transcriptomics identified *PIEZO1*, a key mechanotransduction channel, as being consistently down-regulated after sunitinib exposure.

PIEZO1 is a mechanosensitive ion channel essential for EC mechanotransduction, enabling cells to sense shear stress (63, 64) and transduce calcium-dependent signals that regulate vascular development, endothelial integrity, and NO production (65). Disruption of *PIEZO1* has been linked to hypertension and vascular remodeling (46, 47). Our data establish *PIEZO1* down-regulation as a key driver of sunitinib-induced EC dysfunction. Using a doxycycline-inducible *PIEZO1* overexpression system in iPSC-ECs, we found that restoring *PIEZO1* rescued endothelial function, preserved transcriptional identity, and attenuated sunitinib toxicity. Similarly, pharmacological activation with Yoda1, a *PIEZO1* agonist, restored mechanotransduction and NO production *in vitro* and prevented hypertension and impaired vascular reactivity *in vivo*. *PIEZO1* restoration also suppressed endothelial-to-mesenchymal transition and fibrosis triggered by sunitinib. Although these findings highlight *PIEZO1* as a central regulator of vascular homeostasis, knockdown experiments revealed that additional mechanisms such as oxidative stress, VEGFR signaling disruption, or impaired paracrine communication may contribute to the broader endothelial dysfunction induced by sunitinib.

VEGFR-TKIs such as sunitinib have been linked to severe cardiotoxicities, including reduced LVEF, myocardial infarction, and heart failure. Clinical studies report that 7 to 15% of TKI-treated patients develop symptomatic heart failure (14, 23, 50), and more than 30% exhibit abnormal global longitudinal strain, an early marker of systolic dysfunction (66). Consistent with these findings, 6 of 28 patients in our cohort showed reduced LVEF on long-term follow-up. Although sunitinib-induced cardiomyopathy is often described as reversible (20, 51), the mechanisms driving persistent dysfunction remain poorly defined. Some animal studies suggest direct cardiotoxic effects, with left ventricular impairment observed within 24 hours of sunitinib exposure (67). However, most patients with severe LVEF reduction also develop grade 3 hypertension, supporting a close link between vascular dysfunction and cardiac impairment. Moreover, endothelial dysfunction has been implicated in chemotherapy-related cardiotoxicity more broadly (68), suggesting that endothelial injury may be a critical upstream driver of TKI-associated cardiac dysfunction.

Similar to hypertension, the loss of *PIEZO1* function has been associated with cardiac fibrosis and hypertrophy (46, 47). We therefore

hypothesized that sunitinib-induced disruption of endothelial mechanotransduction, manifesting as hypertension, contributes to long-term cardiac dysfunction. In mice, sunitinib exposure led to persistent reductions in LVEF and FS even after treatment cessation, effects prevented by cotreatment with Yoda1. Multiomic profiling (snRNA-seq and snATAC-seq) of cardiac tissues revealed down-regulation of pathways governing conduction and contractility and up-regulation of chromatin remodeling programs in sunitinib-treated hearts, all of which were reversed by Yoda1. Integration of these datasets highlighted *Tns1* and *Fgfr2*, genes linked to myofibroblast differentiation and ECM formation, as key regulators up-regulated by sunitinib and suppressed with Yoda1. At the protein level, serum biomarkers of cardiac stress were elevated by sunitinib (cTnT and NT-proBNP) and normalized by Yoda1, reinforcing the cardioprotective effect of *PIEZO1* activation. Our engineered human CO model provided complementary mechanistic validation: COs containing both iPSC-ECs and iPSC-CMs developed contractile and calcium handling defects, alongside increased cTnT release, after sunitinib exposure, all of which were rescued by Yoda1. In contrast, CM-only organoids showed no dysfunction, underscoring the role of ECs in driving CM injury. Inducible *PIEZO1* overexpression in iPSC-ECs was sufficient to restore endothelial function and preserve EC-CM cross-talk, confirming that endothelial *PIEZO1* disruption is a causal determinant of sunitinib-induced cardiac dysfunction.

Our study has several limitations. Although our combination of patient-derived iPSC models, mouse experiments, and human COs provided mechanistic insight into endothelial and cardiac dysfunction, these systems do not fully capture the complexity of clinical TKI exposure. iPSC-derived ECs and CMs represent immature phenotypes and lack the multicellular and hormonal interactions of adult tissues. Similarly, the mouse model captures key hemodynamic and molecular features but does not reflect the comorbidities, tumor environment, or treatment duration encountered in patients. The concentrations and duration of sunitinib and Yoda1 exposure may not precisely mirror human pharmacokinetics, and Yoda1 remains a preclinical tool compound. Last, COs, although useful for modeling EC-CM cross-talk, lack immune and systemic inputs relevant to cardiotoxicity. Future studies using more physiologically mature and multicellular human models with longer-term exposure paradigms will be important to translate these findings to the clinic.

In summary, this study demonstrates that VEGFR-TKI-induced cardiotoxicity is driven by endothelial dysfunction and impaired mechanotransduction, mediated in part by down-regulation of the mechanosensitive ion channel *PIEZO1*. Using patient-derived iPSC models, mouse studies, and human COs, we show that sunitinib disrupts endothelial function, promotes hypertension and fibrosis, and impairs CM performance through the loss of EC-CM cross-talk. Restoring *PIEZO1* activity, either pharmacologically with Yoda1 or genetically via inducible overexpression, rescued endothelial signaling, preserved cardiac function, and prevented maladaptive remodeling (fig. S15). These findings position endothelial mechanotransduction as a central determinant of chemotherapy-related cardiovascular toxicity and identify *PIEZO1* as a promising therapeutic target. Future efforts to develop clinically viable *PIEZO1* modulators and to evaluate *PIEZO1* as a biomarker of vascular injury may offer previously unexplored strategies to prevent TKI-associated cardiotoxicity and improve long-term cardiovascular health in patients with cancer.

MATERIALS AND METHODS

Study design

This study investigated the role of endothelial mechanotransduction in mediating vascular and cardiac injury after TKI treatment. The overall objective was to determine how the disruption of the mechanosensitive ion channel PIEZO1 contributes to endothelial dysfunction, hypertension, and cardiotoxicity induced by the VEGFR-targeting TKI sunitinib and to evaluate pharmacological and genetic strategies to restore PIEZO1 activity. The study design incorporated patient-specific iPSC-derived endothelial and cardiac models, *in vivo* murine studies, and human engineered COs. All human studies were conducted under a Stanford University Institutional Review Board-approved protocol. Twenty-eight patients receiving TKI therapy and five HCs were enrolled after informed consent. Inclusion criteria required prior TKI exposure and a clinical diagnosis of vasculotoxicity, including hypertension, defined according to American College of Cardiology/American Heart Association guidelines (systolic/diastolic blood pressure \geq 140/90 mmHg). Patient samples were deidentified in compliance with Health Insurance Portability and Accountability Act regulations. Animal procedures were performed in accordance with protocols approved by the Stanford University Administrative Panel on Laboratory Animal Care. C57BL/6J mice were randomly assigned to treatment groups (vehicle, sunitinib, or sunitinib + Yoda1). Sample sizes (8 to 12 mice per group) were based on prior studies to ensure sufficient statistical power (>80%). Investigators were blinded to treatment allocation during data collection and analysis. End points were predefined and included vascular reactivity, blood pressure, endothelial function, and cardiac performance by echocardiography. For *in vitro* studies, experiments were conducted using independent iPSC-EC and iPSC-CM lines, each performed with at least three biological replicates. Statistical tests, sample sizes (n), number of replicates (N), and uncertainty measures are reported in the corresponding figure legends. Detailed experimental procedures are described in Supplementary Materials and Methods.

EndoPAT assessment

Clinical endothelial function was assessed by digital plethysmography using the noninvasive EndoPAT2000 system (Itamar Medical Ltd.). Detailed procedures are provided in the Supplementary Materials. Endothelial function was expressed as the RHI, calculated as the postocclusion-to-preocclusion peripheral arterial tone (PAT) signal ratio in the occluded arm, normalized to the contralateral control arm and corrected for baseline vascular tone. An RHI value $>$ 1.67 was considered indicative of normal endothelial function, whereas RHI \leq 1.67 was classified as abnormal endothelial function.

iPSC-EC differentiation

EC differentiation was initiated when iPSCs reached ~75% confluence by switching from StemMACS iPS-Brew XF medium to RPMI-B27 without insulin, supplemented with 6 μ M CHIR99021 (Selleck Chemicals) for 2 days. The medium was then replaced with 2 μ M CHIR99021 for an additional 2 days. From day 5 to day 12, cells were cultured in EGM2 medium (Lonza), changed every 2 days, supplemented with VEGF (50 ng/ml; PeproTech), fibroblast growth factor 2 (20 ng/ml; PeproTech), and 10 μ M transforming growth factor- β inhibitor (SB431542) (Selleck Chemicals). On day 12, cells were dissociated with TrypLE Express (Sigma-Aldrich) for 5 min at 37°C and sorted for CD144 $^+$ populations using magnetic microbeads and magnetic-activated cell sorting columns (Miltenyi Biotec) according

to the manufacturer's instructions. Sorted CD144 $^+$ cells were seeded onto 0.2% gelatin-coated plates and maintained in EGM2 medium supplemented with 10 μ M SB431542. iPSC-ECs were used experimentally up to passage 2 (69, 70).

Mouse treatments and blood pressure assessment

Male and female C57BL/6J mice (8 to 12 weeks old, 25 to 30 g) were used for all *in vivo* studies. Mice were randomly assigned to receive vehicle, sunitinib (40 mg/kg orally, Selleckchem) for 21 days, or sunitinib (40 mg/kg orally) and Yoda1 (5 mg/kg intraperitoneally, TOCRIS) for 21 days. After treatment, animals were left untreated for 90 days, and hearts and aortas were collected on days 21 and 111 for analysis. Blood pressure was monitored noninvasively using the CODA tail-cuff system (Kent Scientific) on days 7, 14, 21, and 90, with mice pretrained to minimize stress. Additional procedural details are provided in the Supplementary Materials.

Fabrication of COs

COs were generated using iPSC-CMs alone or in combination with iPSC-ECs. For coculture organoids, iPSC-CMs and iPSC-ECs were dissociated with TrypLE Express (Sigma-Aldrich) and combined at a 70:30 ratio (CM:EC). The resulting cell suspension was seeded into agarose molds (Microtissues Inc.) containing a 9-by-9 microwell array at a final density of 1×10^6 cells/ml. Over 48 hours, the cells sedimented into the microwells and self-assembled into three-dimensional organoids. The spontaneously beating COs were maintained in RPMI-B27 medium supplemented with insulin at 37°C in a humidified atmosphere of 5% CO₂.

Statistical analysis

All cell culture experiments were performed in triplicate, with at least two technical replicates per experiment. For comparisons between two groups, significance was assessed using a two-tailed Student's *t* test, whereas comparisons among more than two groups were analyzed using a one-way analysis of variance (ANOVA) with appropriate post hoc testing. Data were analyzed using Prism (GraphPad Software) and are presented as the means \pm SEM, unless otherwise indicated. A *P* value of <0.05 was considered statistically significant.

Supplementary Materials

The PDF file includes:

Materials and Methods

Figs. S1 to S15

Tables S1 to S3

Other Supplementary Material for this manuscript includes the following:

Data file S1

MDAR Reproducibility Checklist

REFERENCES AND NOTES

- D. T. Michaeli, J. C. Michaeli, T. Michaeli, Advances in cancer therapy: Clinical benefit of new cancer drugs. *Aging* **15**, 5232–5234 (2023).
- A. Jemal, E. P. Simard, C. Dorell, A. M. Noone, L. E. Markowitz, B. Kohler, C. Eheman, M. Saraiya, P. Bandi, D. Saslow, K. A. Cronin, M. Watson, M. Schiffman, S. J. Henley, M. J. Schymura, R. N. Anderson, D. Yankey, B. K. Edwards, Annual Report to the Nation on the Status of Cancer, 1975–2009, featuring the burden and trends in human papillomavirus(HPV)-associated cancers and HPV vaccination coverage levels. *J. Natl. Cancer Inst.* **105**, 175–201 (2013).
- J. J. Mosleh, M. Deininger, Tyrosine kinase inhibitor-associated cardiovascular toxicity in chronic myeloid leukemia. *J. Clin. Oncol.* **33**, 4210–4218 (2015).

4. S. Shyam Sunder, U. C. Sharma, S. Pokharel, Adverse effects of tyrosine kinase inhibitors in cancer therapy: Pathophysiology, mechanisms and clinical management. *Signal Transduct. Target. Ther.* **8**, 262 (2023).
5. K. B. Orrico, Basic concepts of cancer genetics and receptor tyrosine kinase inhibition for pharmacists. A narrative review. *J. Oncol. Pharm. Pract.* **29**, 1187–1195 (2023).
6. N. Sayegh, J. Yirerong, N. Agarwal, D. Addison, M. Fradley, J. Cortes, N. L. Weintraub, N. Sayed, G. Raval, A. Guha, Cardiovascular toxicities associated with tyrosine kinase inhibitors. *Curr. Cardiol. Rep.* **25**, 269–280 (2023).
7. J. Herrmann, Tyrosine kinase inhibitors and vascular toxicity: Impetus for a classification system? *Curr. Oncol. Rep.* **18**, 33 (2016).
8. B. Franczyk, J. Rysz, J. Ławiński, A. Ciałkowska-Rysz, A. Gluba-Brzózka, Cardiotoxicity of selected vascular endothelial growth factor receptor tyrosine kinase inhibitors in patients with renal cell carcinoma. *Biomedicine* **11**, 181 (2023).
9. D. Mihalcea, H. Memis, S. Mihaila, D. Vinereanu, Cardiovascular toxicity induced by vascular endothelial growth factor inhibitors. *Life* **13**, 366 (2023).
10. T. Wojcik, E. Szczesny, S. Chlopicki, Detrimental effects of chemotherapeutics and other drugs on the endothelium: A call for endothelial toxicity profiling. *Pharmacol. Rep.* **67**, 811–817 (2015).
11. A. Soultati, G. Mountzios, C. Avgerinou, G. Papaxoinis, D. Pectasides, M. A. Dimopoulos, C. Papadimitriou, Endothelial vascular toxicity from chemotherapeutic agents: Preclinical evidence and clinical implications. *Cancer Treat. Rev.* **38**, 473–483 (2012).
12. N. Camarda, R. Travers, V. K. Yang, C. London, I. Z. Jaffe, VEGF receptor inhibitor-induced hypertension: Emerging mechanisms and clinical implications. *Curr. Oncol. Rep.* **24**, 463–474 (2022).
13. R. J. Travers, A. Stepanian, I. Z. Jaffe, Endothelium as a source of cardiovascular toxicity from antitumor kinase inhibitors. *Arterioscler. Thromb. Vasc. Biol.* **44**, 2143–2153 (2024).
14. M. L. Telli, R. M. Witteles, G. A. Fisher, S. Srinivas, Cardiotoxicity associated with the cancer therapeutic agent sunitinib malate. *Ann. Oncol.* **19**, 1613–1618 (2008).
15. M. H. W. Kappers, V. J. de Beer, Z. Zhou, A. H. J. Danser, S. Sleijfer, D. J. Duncker, A. H. van den Meiracker, D. Merkus, Sunitinib-induced systemic vasoconstriction in swine is endothelin mediated and does not involve nitric oxide or oxidative stress. *Hypertension* **59**, 151–157 (2012).
16. M. J. Davis, S. Earley, Y.-S. Li, S. Chien, Vascular mechanotransduction. *Physiol. Rev.* **103**, 1247–1421 (2023).
17. S. Chatterjee, Endothelial mechanotransduction, redox signaling and the regulation of vascular inflammatory pathways. *Front. Physiol.* **9**, 524 (2018).
18. A. González, S. Ravassa, B. López, M. U. Moreno, J. Beaumont, G. San José, R. Querejeta, A. Bayés-Genís, J. Diez, Myocardial remodeling in hypertension. *Hypertension* **72**, 549–558 (2018).
19. J. D. Cornwell, J. C. McDermott, MEF2 in cardiac hypertrophy in response to hypertension. *Trends Cardiovasc. Med.* **33**, 204–212 (2023).
20. I. Uraizee, S. Cheng, J. Moslehi, Reversible cardiomyopathy associated with sunitinib and sorafenib. *N. Engl. J. Med.* **365**, 1649–1650 (2011).
21. R. Kerkela, K. C. Woulfe, J. B. Durand, R. Vagnozzi, D. Kramer, T. F. Chu, C. Beahm, M. H. Chen, T. Force, Sunitinib-induced cardiotoxicity is mediated by off-target inhibition of AMP-activated protein kinase. *Clin. Transl. Sci.* **2**, 15–25 (2009).
22. H. Cheng, G. Kari, A. P. Dicker, U. Rodeck, W. J. Koch, T. Force, A novel preclinical strategy for identifying cardiotoxic kinase inhibitors and mechanisms of cardiotoxicity. *Circ. Res.* **109**, 1401–1409 (2011).
23. T. F. Chu, M. A. Rupnick, R. Kerkela, S. M. Dallabrida, D. Zurkowski, L. Nguyen, K. Woulfe, E. Pravda, F. Cassiola, J. Desai, S. George, D. M. Harris, N. S. Ismail, J. H. Chen, F. J. Schoen, A. D. van den Abbeele, G. D. Demetri, T. Force, M. H. Chen, J. A. Morgan, Cardiotoxicity associated with tyrosine kinase inhibitor sunitinib. *Lancet* **370**, 2011–2019 (2007).
24. A. Sharma, P. W. Burridge, W. L. McKeithan, R. Serrano, P. Shukla, N. Sayed, J. M. Churko, T. Kitani, H. Wu, A. Holmström, E. Matsa, Y. Zhang, A. Kumar, A. C. Fan, J. C. del Alamo, S. M. Wu, J. J. Moslehi, M. Mercola, J. C. Wu, High-throughput screening of tyrosine kinase inhibitor cardiotoxicity with human induced pluripotent stem cells. *Sci. Transl. Med.* **9**, eaaf2584 (2017).
25. D. R. Talbert, K. R. Doherty, P. B. Trusk, D. M. Moran, S. A. Shell, S. Bacus, A multi-parameter in vitro screen in human stem cell-derived cardiomyocytes identifies ponatinib-induced structural and functional cardiac toxicity. *Toxicol. Sci.* **143**, 147–155 (2014).
26. X. Zhu, K. Stergiopoulos, S. Wu, Risk of hypertension and renal dysfunction with an angiogenesis inhibitor sunitinib: Systematic review and meta-analysis. *Acta Oncol.* **48**, 9–17 (2009).
27. W. Li, K. Croce, D. P. Steensma, D. F. McDermott, O. Ben-Yehuda, J. Moslehi, Vascular and metabolic implications of novel targeted cancer therapies. *J. Am. Coll. Cardiol.* **66**, 1160–1178 (2015).
28. Y. Yang, Y. Zhang, Z. Cao, H. Ji, X. Yang, H. Iwamoto, E. Wahlberg, T. Länne, B. Sun, Y. Cao, Anti-VEGF- and anti-VEGF receptor-induced vascular alteration in mouse healthy tissues. *Proc. Natl. Acad. Sci.* **110**, 12018–12023 (2013).
29. M. H. W. Kappers, J. H. M. van Esch, W. Sluiter, S. Sleijfer, A. H. J. Danser, A. H. van den Meiracker, Hypertension induced by the tyrosine kinase inhibitor sunitinib is associated with increased circulating endothelin-1 levels. *Hypertension* **56**, 675–681 (2010).
30. S. Waliany, K. L. Sainani, L. S. Park, C. A. Zhang, S. Srinivas, R. M. Witteles, Increase in blood pressure associated with tyrosine kinase inhibitors targeting vascular endothelial growth factor. *JACC CardioOncol.* **1**, 24–36 (2019).
31. U. Raff, C. Ott, S. John, B. M. W. Schmidt, E. H. Fleischmann, R. E. Schmieder, Nitric oxide and reactive hyperemia: Role of location and duration of ischemia. *Am. J. Hypertens.* **23**, 865–869 (2010).
32. N. Sayed, C. Liu, M. Ameen, F. Himmati, J. Z. Zhang, S. Khanamiri, J. R. Moonen, A. Wnorowski, L. Cheng, J. W. Rhee, S. Gaddam, K. C. Wang, K. Sallam, J. H. Boyd, Y. J. Woo, M. Rabinovitch, J. C. Wu, Clinical trial in a dish using iPSCs shows lovastatin improves endothelial dysfunction and cellular cross-talk in LMNA cardiomyopathy. *Sci. Transl. Med.* **12**, eaax9276 (2020).
33. N. Sayed, C. Liu, J. C. Wu, Translation of human-induced pluripotent stem cells: From clinical trial in a dish to precision medicine. *J. Am. Coll. Cardiol.* **67**, 2161–2176 (2016).
34. D. Thomas, S. Shenoy, N. Sayed, Building multi-dimensional induced pluripotent stem cells-based model platforms to assess cardiotoxicity in cancer therapies. *Front. Pharmacol.* **12**, 607364 (2021).
35. N. Sayed, W. T. Wong, F. Ospino, S. Meng, J. Lee, A. Jha, P. Dexheimer, B. J. Aronow, J. P. Cooke, Transdifferentiation of human fibroblasts to endothelial cells: Role of innate immunity. *Circulation* **131**, 300–309 (2015).
36. E. Tzima, M. Irani-Tehrani, W. B. Kiosses, E. Dejana, D. A. Schultz, B. Engelhardt, G. Cao, H. DeLisser, M. A. Schwartz, A mechanosensory complex that mediates the endothelial cell response to fluid shear stress. *Nature* **437**, 426–431 (2005).
37. B. G. Coon, N. Baeyens, J. Han, M. Budatha, T. D. Ross, J. S. Fang, S. Yun, J. L. Thomas, M. A. Schwartz, Intramembrane binding of VE-cadherin to VEGFR2 and VEGFR3 assembles the endothelial mechanosensory complex. *J. Cell Biol.* **208**, 975–986 (2015).
38. I. A. Tamargo, K. I. Baek, Y. Kim, C. Park, H. Jo, Flow-induced reprogramming of endothelial cells in atherosclerosis. *Nat. Rev. Cardiol.* **20**, 738–753 (2023).
39. P. S. Hall, L. C. Harshman, S. Srinivas, R. M. Witteles, The frequency and severity of cardiovascular toxicity from targeted therapy in advanced renal cell carcinoma patients. *JACC Heart Fail.* **1**, 72–78 (2013).
40. A. Manhas, D. Tripathi, D. Thomas, N. Sayed, Cardiovascular toxicity in cancer therapy: Protecting the heart while combating cancer. *Curr. Cardiol. Rep.* **26**, 953–971 (2024).
41. T. J. Stuhlmiller, J. S. Zawistowski, X. Chen, N. Scialy, S. P. Angus, S. T. Hicks, T. L. Parry, W. Huang, J. Y. Beak, M. S. Willis, G. L. Johnson, B. C. Jensen, Kinome and transcriptome profiling reveal broad and distinct activities of erlotinib, sunitinib, and sorafenib in the mouse heart and suggest cardiotoxicity from combined signal transducer and activator of transcription and epidermal growth factor receptor inhibition. *J. Am. Heart Assoc.* **6**, e006635 (2017).
42. C. Schem, D. Bauerschlag, S. Bender, A. C. Lorenzen, D. Loermann, S. Hamann, F. Rösel, H. Kalhoff, C. C. Glüer, W. Jonat, S. Tiwari, Preclinical evaluation of Sunitinib as a single agent in the prophylactic setting in a mouse model of bone metastases. *BMC Cancer* **13**, 32 (2013).
43. S. B. Nukala, J. Jousma, G. Yan, Z. Han, Y. Kwon, Y. Cho, C. Liu, K. Gagnon, S. Pinho, J. Rehman, N. Y. Shao, S. B. Ong, W. H. Lee, S. G. Ong, Modulation of lncRNA links endothelial glycocalyx to vascular dysfunction of tyrosine kinase inhibitor. *Cardiovasc. Res.* **119**, 1997–2013 (2023).
44. J. Sourdon, C. Facchini, A. Certain, T. Viel, B. Robin, F. Lager, C. Marchiol, D. Balvay, T. Yoganathan, J. Favier, P. L. Tharaux, N. Dhaun, G. Renault, B. Tavitian, Sunitinib-induced cardiac hypertrophy and the endothelin axis. *Theranostics* **11**, 3830–3838 (2021).
45. S. Khanamiri, J. W. Rhee, D. T. Paik, I. Y. Chen, C. Liu, N. Sayed, Marked vascular dysfunction in a case of peripartum cardiomyopathy. *J. Vasc. Res.* **56**, 11–15 (2019).
46. S. Wang, R. Chennupati, H. Kaur, A. Iring, N. Wettschureck, S. Offermanns, Endothelial cation channel PIEZO1 controls blood pressure by mediating flow-induced ATP release. *J. Clin. Invest.* **126**, 4527–4536 (2016).
47. D. Douguet, A. Patel, A. Xu, P. M. Vanhoutte, E. Honoré, Piezo ion channels in cardiovascular mechanobiology. *Trends Pharmacol. Sci.* **40**, 956–970 (2019).
48. R. Syeda, J. Xu, A. E. Dubin, B. Coste, J. Mathur, T. Huynh, J. Matzen, J. Lao, D. C. Tully, I. H. Engels, H. M. Petrossi, A. M. Schumacher, M. Montal, M. Bandell, A. Patapoutian, Chemical activation of the mechanotransduction channel Piezo1. *eLife* **4**, e07369 (2015).
49. J. E. Davies, D. Lopresto, B. H. R. Apta, Z. Lin, W. Ma, M. T. Harper, Using Yoda-1 to mimic laminar flow in vitro: A tool to simplify drug testing. *Biochem. Pharmacol.* **168**, 473–480 (2019).
50. G. Di Lorenzo, R. Autorino, G. Bruni, G. Cartenì, E. Ricevuto, M. Tudini, C. Fiorella, C. Romano, M. Aieta, A. Giordano, M. Giuliano, A. Gonnella, C. De Nunzio, M. Rizzo, V. Montesarchio, M. Ewer, S. De Placido, Cardiovascular toxicity following sunitinib therapy in metastatic renal cell carcinoma: A multicenter analysis. *Ann. Oncol.* **20**, 1535–1542 (2009).
51. M. S. Ewer, S. M. Lippman, Type II chemotherapy-related cardiac dysfunction: Time to recognize a new entity. *J. Clin. Oncol.* **23**, 2900–2902 (2005).

52. A. Y. Khakoo, C. M. Kassiotis, N. Tannir, J. C. Plana, M. Halushka, C. Bickford, J. Trent II, J. C. Champion, J. B. Durand, D. J. Lenihan, Heart failure associated with sunitinib malate. *Cancer* **112**, 2500–2508 (2008).
53. Y. Zhang, L. Ling, A. Ajay D/O Ajayakumar, Y. M. Eio, A. J. van Wijnen, V. Nurcombe, S. M. Cool, FGFR2 accommodates osteogenic cell fate determination in human mesenchymal stem cells. *Gene* **818**, 146199 (2022).
54. D. Ranieri, M. Nanni, F. Persechino, M. R. Torrisi, F. Belleudi, Role of PKC ϵ in the epithelial-mesenchymal transition induced by FGFR2 isoform switch. *Cell Commun. Signal.* **18**, 76 (2020).
55. D. Thomas, V. A. de Jesus Perez, N. Sayed, An evidence appraisal of heart organoids in a dish and commensurability to human heart development in vivo. *BMC Cardiovasc. Disord.* **22**, 122 (2022).
56. D. Thomas, C. Noishiki, S. Gaddam, D. Wu, A. Manhas, Y. Liu, D. Tripathi, N. Kathale, S. S. Adkar, J. Garhyani, C. Liu, B. Xu, E. G. Ross, R. L. Dalman, K. C. Wang, A. E. Oro, K. Sallam, J. T. Lee, J. C. Wu, N. Sayed, CCL2-mediated endothelial injury drives cardiac dysfunction in long COVID. *Nat. Cardiovasc. Res.* **3**, 1249–1265 (2024).
57. K. Sallam, D. Thomas, S. Gaddam, N. Lopez, A. Beck, L. Beach, A. J. Rogers, H. Zhang, I. Y. Chen, M. Ameen, W. Hiesinger, J. J. Teuteberg, J. W. Rhee, K. C. Wang, N. Sayed, J. C. Wu, Modeling effects of immunosuppressive drugs on human hearts using induced pluripotent stem cell-derived cardiac organoids and single-cell RNA sequencing. *Circulation* **145**, 1367–1369 (2022).
58. T. Force, D. S. Krause, R. A. Van Etten, Molecular mechanisms of cardiotoxicity of tyrosine kinase inhibition. *Nat. Rev. Cancer* **7**, 332–344 (2007).
59. B. Liu, F. Ding, Y. Liu, G. Xiong, T. Lin, D. He, Y. Zhang, D. Zhang, G. Wei, Incidence and risk of hypertension associated with vascular endothelial growth factor receptor tyrosine kinase inhibitors in cancer patients: A comprehensive network meta-analysis of 72 randomized controlled trials involving 30013 patients. *Oncotarget* **7**, 67661–67673 (2016).
60. M. H. Chen, R. Kerkelä, T. Force, Mechanisms of cardiac dysfunction associated with tyrosine kinase inhibitor cancer therapeutics. *Circulation* **118**, 84–95 (2008).
61. J. Sourdon, F. Lager, T. Viel, D. Balvay, R. Moorhouse, E. Bennana, G. Renault, P. L. Tharaux, N. Dhaun, B. Tavitian, Cardiac metabolic deregulation induced by the tyrosine kinase receptor inhibitor sunitinib is rescued by endothelin receptor antagonism. *Theranostics* **7**, 2757–2774 (2017).
62. D. Huang, Y. Ding, Y. Li, W. M. Luo, Z. F. Zhang, J. Snider, K. VandenBeldt, C. N. Qian, B. T. Teh, Sunitinib acts primarily on tumor endothelium rather than tumor cells to inhibit the growth of renal cell carcinoma. *Cancer Res.* **70**, 1053–1062 (2010).
63. S. S. Ranade, Z. Qiu, S. H. Woo, S. S. Hur, S. E. Murthy, S. M. Cahalan, J. Xu, J. Mathur, M. Bandell, B. Coste, Y. S. J. Li, S. Chien, A. Patapoutian, Piezo1, a mechanically activated ion channel, is required for vascular development in mice. *Proc. Natl. Acad. Sci. U.S.A.* **111**, 10347–10352 (2014).
64. B. Coste, J. Mathur, M. Schmidt, T. J. Earley, S. Ranade, M. J. Petrus, A. E. Dubin, A. Patapoutian, Piezo1 and Piezo2 are essential components of distinct mechanically activated cation channels. *Science* **330**, 55–60 (2010).
65. B. Coste, P. Delmas, PIEZO ion channels in cardiovascular functions and diseases. *Circ. Res.* **134**, 572–591 (2024).
66. L. F. Nhola, S. S. Abdelmoneim, H. R. Villarraga, M. Kohli, A. Grothey, K. A. Bordun, M. Cheung, R. Best, D. Cheung, R. Huang, S. Barros-Gomes, M. Pitz, P. K. Singal, D. S. Jassal, S. L. Mulvagh, Echocardiographic assessment for the detection of cardiotoxicity due to vascular endothelial growth factor inhibitor therapy in metastatic renal cell and colorectal cancers. *J. Am. Soc. Echocardiogr.* **32**, 267–276 (2019).
67. K.-A. Bordun, S. Premecz, M. daSilva, S. Mandal, V. Goyal, T. Glavinovic, M. Cheung, D. Cheung, C. W. White, R. Chaudhary, D. H. Freed, H. R. Villarraga, J. Herrmann, M. Kohli, A. Ravandi, J. Thliveris, M. Pitz, P. K. Singal, S. Mulvagh, D. S. Jassal, The utility of cardiac biomarkers and echocardiography for the early detection of bevacizumab- and sunitinib-mediated cardiotoxicity. *Am. J. Physiol. Heart Circ. Physiol.* **309**, H692–H701 (2015).
68. C. Ching, D. Gustafson, P. Thavendiranathan, J. E. Fish, Cancer therapy-related cardiac dysfunction: Is endothelial dysfunction at the heart of the matter? *Clin. Sci.* **135**, 1487–1503 (2021).
69. N. Sayed, Y. Huang, K. Nguyen, Z. Krejciova-Rajaniemi, A. P. Grawe, T. Gao, R. Tibshirani, T. Hastie, A. Alpert, L. Cui, T. Kuznetsova, Y. Rosenberg-Hasson, R. Ostan, D. Monti, B. Lehallier, S. S. Shen-Orr, H. T. Maeker, C. L. Dekker, T. Wyss-Coray, C. Franceschi, V. Jojic, F. Haddad, J. G. Montoya, J. C. Wu, M. M. Davis, D. Furman, An inflammatory aging clock (iAge) based on deep learning tracks multimorbidity, immunosenescence, frailty and cardiovascular aging. *Nat. Aging* **1**, 598–615 (2021).
70. C. Liu, M. Shen, W. L. W. Tan, I. Y. Chen, Y. Liu, X. Yu, H. Yang, A. Zhang, Y. Liu, M. T. Zhao, M. Ameen, M. Zhang, E. R. Gross, L. S. Qi, N. Sayed, J. C. Wu, Statins improve endothelial function via suppression of epigenetic-driven EndMT. *Nat. Cardiovasc. Res.* **2**, 467–485 (2023).

Acknowledgments: We thank N. Leeper for the EndoPAT machine, D. Wagh for assistance with snMultiome experiments; M. Ameen for technical support, and all recruited patients for donating samples and time. Schematic figures were created using <https://biorender.com>.

Funding: This study was supported by research grants from the National Institutes of Health (R01 HL158641 to N.S., R01 HL161002 to N.S., and K01 HL135455 to N.S.), American Heart Association Strategically Focused Research Network grant (869015 to N.S.), Stanford Surgery Seed Grant to N.S., National Institutes of Health (R01 HL141851 to J.C.W., R01 HL145676 to J.C.W., R01 HL150693 to J.C.W., and R01 HL1476822 to J.C.W.), and AHA award (23POST1020812 to A.M. and 25CDA1456151 to A.M.). **Author contributions:** N.S. conceptualized the study, designed all experiments, and supervised the overall project. N.S. and A.M. analyzed the data and wrote the manuscript. A.M., C.N., and D.W. performed most of the in vitro experiments, including iPSC-EC functional assays, flow-mediated shear stress studies, and transcriptional profiling. C.N. contributed to iPSC-EC differentiation and endothelial functional assays and assisted with organoid experiments. Y.L. conducted bioinformatic analyses including bulk RNA-seq, scRNA-seq, and snMultiome analyses assisted by D.W. D.Tr. assisted with 10x Genomics experiments and nucleus preparation for multiomic sequencing. S.M. and L.L. generated iPSC-EC and iPSC-CM lines and maintained pluripotent stem cell cultures. D.Th. fabricated and optimized human COs and assisted with contractility and calcium-handling assays. D.S. provided expertise for mouse CM isolations. M.L.T. and P.C. recruited TKI-treated patients, collected clinical samples, and assisted with clinical data interpretation. I.Y.C. and K.S. contributed to clinical studies, including patient evaluation, phenotyping, and vascular testing. V.C., A.G., P.K.N., K.S., and J.C.W. provided scientific input, edited the manuscript, and contributed to interpretation of the data. All authors discussed the results, reviewed the manuscript, and approved the final version. **Competing interests:** N.S. is an inventor on a pending patent application related to this work entitled “Treatment of cardiovascular complications due to chemotherapy” (US application no. 63/748,873). J.C.W. is a cofounder and scientific advisory board (SAB) member of Greenstone Biosciences; this relationship is unrelated to the present study. The other authors declare that they have no competing interests. **Data and materials availability:** All data associated with this study are present in the paper or the Supplementary Materials. Raw bulk RNA-seq, scRNA-seq, and snMultiome data have been deposited in GEO under accession numbers GSE309753, GSE309754, and GSE309795. All materials are available upon request, and the following materials require completion of a materials transfer agreement (MTA): patient-specific iPSC lines.

Submitted 13 January 2025

Resubmitted 30 July 2025

Accepted 19 November 2025

Published 17 December 2025

10.1126/scitranslmed.adv9403